IPP-Report

Max-Planck-Institut
für Plasmaphysik

Emanuel Huett

Determination of 2D Plasma Parameters with Filtered Cameras

IPP 2022-05
April 2022


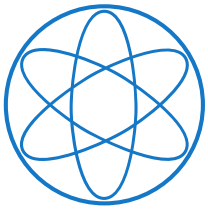


Report Based on a Master's Thesis in Physics at
Technische Universität München

Determination of 2D Plasma Parameters with Filtered Cameras

An Application to the X-Point Radiator Regime in ASDEX Upgrade

presented by

Emanuel Huett

Lausanne, 23 April 2022

First Promoter:	Prof. Dr. Ulrich Stroth
Second Promoter:	Prof. Dr. Rudolf Neu
Supervisor:	Dr. Marco Cavedon, Dr. Tilmann Lunt

Determination of 2D Plasma Parameters with Filtered Cameras

An Application to the X-Point Radiator Regime in ASDEX Upgrade

Emanuel Huett

Abstract

The potential of filtered cameras to gain new insights into the phenomena occurring in a tokamak has increased drastically with available computing power and computational methods over the last years. In this work, a three-step method for the determination of 2D plasma parameters in a toroidally symmetric tokamak is presented. The cameras are calibrated in a first step and measure hydrogen Balmer α, β, and γ spectral line emissions. In a second step, tomographic methods are applied to reconstruct the distribution of the emitted light from a toroidally symmetric plasma. Finally, plasma parameters are inferred from these reconstructed profiles.

The method is tested on the data from 2D simulations with the scrape-off layer transport code SOLPS. Therefore, photo-realistic camera images are generated using detailed construction drawings of the tokamak. Metallic reflections are not only modeled for these artificial images, but are considered for the reconstruction as well. The feasibility to determine 2D electron density and temperature experimentally is tested for a technical low temperature plasma, generated only by electron cyclotron resonance heating.

The method has been successfully applied to dedicated discharges with an X-point radiator, one of the most promising scenarios for power exhaust control in a fusion reactor. An analysis of a first discharge indicates that a well-developed X-point radiator cools the plasma to a point where recombination dominates the Balmer line emissions. This finding is supported by a SOLPS simulation and other diagnostics. A second discharge with similar external parameters, but a smaller toroidal magnetic field showed a different emission pattern. These discrepancies allow studying parametric dependencies of theoretical X-point radiator models.

Bestimmung von 2D-Plasmaparametern mit gefilterten Kameras

Eine Anwendung auf das X-Punkt-Strahler-Regime in ASDEX Upgrade

Emanuel Hütt

Kurzzusammenfassung

Das Potenzial, mittels gefilterter Kameras neue Erkenntnisse über die in einem Tokamak auftretenden Phänomene zu gewinnen, ist in den letzten Jahren mit der nun verfügbaren Rechenleistung und Rechenmethoden drastisch gestiegen. In dieser Arbeit wird eine dreiteilige Methode zur Bestimmung von 2D-Plasmaparametern mit gefilterten Kameras in einem toroidal symmetrischen Tokamak präsentiert. Die Kameras werden in einem ersten Schritt kalibriert und messen die Balmer Spektrallinien α, β und γ, welche das Wasserstoffplasma im sichtbaren Spektrum emittiert. In einem zweiten Schritt werden tomografische Methoden angewandt, um die toroidal symmetrische Verteilung des emittierten Lichts zu rekonstruieren. Schließlich werden die Plasmaparameter aus den rekonstruierten Emissionen abgeleitet.

Für eine Überprüfung der Methodik werden Kamerabilder aus zweidimensionalen Simulationen mit dem Abschälschicht-Transportcode SOLPS generiert. Unter der Verwendung von 3D-Konstruktionszeichnungen werden fotorealistische Reflektionen modelliert. Diese erscheinen nicht nur in den künstlichen Kamerabildern, vielmehr werden diese auch bei der Rekonstruktion berücksichtigt. Die Möglichkeit 2D Dichte und Temperatur experimentell zu bestimmen wird anhand eines technisches Nidertemperaturplasmas getestet.

Erfolgreich angewandt wurde die Methode auch auf das X-Punkt-Strahler-Regime, eines der vielversprechendsten Szenarien für eine kontrollierte Leistungsabfuhr in einem Fusionsreaktor. Die vorgestellte Analyse einer ersten Entladung zeigt, dass ein weit entwickelter X-Punkt-Strahler das Plasma bis zu einem Punkt abkühlt, an dem die Rekombination die Balmer-Linienemissionen dominiert. Eine SOLPS-Simulation und eine weitere Diagnostik bestätigen diese Erkenntnis. Eine zweite Entladung mit einem kleineren toroidalen Magnetfeld und ansonsten ähnlichen Rahmenbedingungen zeigte ein anderes Emissionsmuster. Dies ermöglicht die Untersuchung der Parameterabhängigkeit von theoretischen Modellen des X-Punkt-Strahlers.

Contents

Chapter 1

Introduction

1.1 Motivation for Fusion Energy

The world energy supply is not only one of the most pressing tasks we are facing today but will continue to be so in the future. "After declining in 2020, electricity demand is expected to increase [significantly] in 2021, pushing consumption well above pre-pandemic levels." [1] The energy demand in developing countries is continuously rising to fulfill basic needs as well as modern-day necessities. "Pressures on the energy system are not going to relent in the coming decades." [1]

Not only are fossil fuels limited, but also due to the harsh reality of climate change, there is an impelling need for sustainable energy sources. In the European Union, electricity production in 2019 originated 39% from burning fossil fuels, 26% from nuclear power plants, and only 35% from renewable energy sources. [2] More efforts have to be made in limiting the energy demand and pushing renewable energy sources.

In order to meet future demands of sustainable energy, nuclear fusion bears an enormous potential. Similar to the sun, a nuclear fusion power plant would fuse hydrogen isotopes into helium. Deuterium is one of the isotopes and largely available in natural water. The second isotope is tritium and can be obtained from lithium in the blanket of the reactor. The two isotopes can be fused at very high temperatures where they are in a state of matter called plasma. In contrast to nuclear fission, nuclear fusion does not produce radioactive waste that is hard to dispose in the long term. Furthermore, a hypothetical fusion accident would not have as an severe impact as the Fukushima nuclear disaster.

In recent decades of research, it became clear how challenging it is to put fusion into practice. An important parameter in approaching reactor conditions is the power enhancement factor Q, which is defined as

$$Q = \frac{P_{fus}}{P_{aux}}. \tag{1.1}$$

It relates the power obtained by fusion reactions P_{fus} to the auxiliary heating

power P_{aux} supplied to the plasma. "Plasma energy breakeven, or $Q = 1$, has never been achieved in a fusion device: the current record is held by the European tokamak JET (UK), which succeeded in generating a Q of 0.67." [3] A formulation of this breakeven in terms of plasma parameters is approximately given by the triple product of plasma density, temperature, and energy confinement time. In other words, a fusion reactor requires a high pressure plasma that is thermally well insulated.

1.2 Magnetic Confinement in the Tokamak

To counteract the expansion of the hot plasma it can be confined with strong magnetic fields. The charged particles comprising the plasma gyrate around the field lines, while freely moving parallel to it. To confine the plasma the field lines are closed in a torus shape. However, a simple toroidal field cannot hold the plasma because an intrinsic gradient in the magnetic field leads to a vertical electric field via the ∇B-drift. If there is an additional poloidal magnetic field the field lines are twisted like a screw thread and the electric field is short-circuited.

The most advanced and promising concept to achieve fusion in a power plant is the tokamak. In this concept the twist is due to a toroidal current in the plasma itself. The twisted field lines form flux surfaces that are nested, i.e. each flux surface encloses a volume with more flux surfaces and the surfaces do not intersect. The confined region of the plasma is limited by the scrape-off layer, where the flux surfaces intersect with the wall of the tokamak. Fig. 1.1 shows a tokamak plasma with an X-point in the magnetic field. The flux surface that contains the X-point is referred to as separatrix and marks the boundary between confined plasma and scrape-off layer. Such a configuration allows to handle the plasma-wall interaction in a remote region at a low plasma temperature. Most of the thermal energy of the plasma that is transported over the separatrix ends up this remote region and needs to be exhausted by the so called divertor. Due to the high power exhaust of the core plasma it is a challenge to operate a reactor without damaging the divertor. However, it is possible to radiate a large portion of the power exhaust in this configuration. Furthermore, this configuration removes impurities effectively and provides a clean plasma. This is particularly important to get rid of the helium ash in a reactor.

A stable plasma is usually observed when the pressure gradient perpendicular to magnetic flux surfaces is small. However, a small perpendicular gradient is associated to low confinement and there is significant turbulent transport across flux surfaces. Low confinement modes (L-mode) are not favorable for a fusion reactor. It was observed in 1982 at ASDEX, the predecessor of ASDEX Upgrade (AUG), that above a certain heating power regimes with higher confinement (H-mode) are accessible. [5] With higher heating power perpendicular pressure gradients increase and strong shear flows are introduced. Such

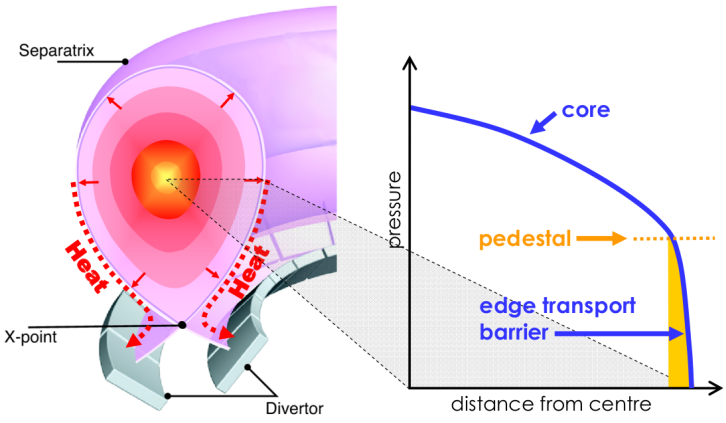

FIGURE 1.1: Geometry of a tokamak in which heat is transferred from the core plasma to the divertor. Transport barriers in the edge lead to a pressure pedestal. Figure taken from [4].

macro-scale zonal flows tear apart small-scale vortices and form a barrier for turbulent transport.

Fig. 1.1 illustrates that the transport barrier is particularly strong in the edge plasma which leads to a pressure pedestal. Since the pressure gradient reinforces the transport barrier the pedestal builds up even further until magnetohydrodynamic modes set in. In this edge localized mode (ELM), part of the plasma energy is released in a sudden burst.

1.3 Related Work with Filtered Cameras

While camera measurements in tokamaks are available since decades, their analysis has proved challenging. The camera images are difficult to interpret because their viewing geometry is complex and the light emitted by the plasma is reflected by the wall. Attempts have been made to tackle these problems since years, for example in AUG toroidally symmetric reflections were considered [6]. In this work, realistic reflections are modeled from 3D construction drawings and in the analyzed experimental data the emitted light is far away from the wall. The neutral density has been a major subject of study [7], it is difficult to estimate and is not determined in this work. Hydrogen emissions in the divertor region have been measured in discharges with high impurity seeding at the TCV tokamak recently. [8] While the XPR is controlled using bolometers in AUG, also filtered cameras are eligible to control an impurity emission front. [9] Bayesian inference has been implemented within a multi-diagnostic approach using also camera measurements. [10] This approach was tested using synthetic diagnostic measurements derived from SOLPS, which is also done in this work.

1.4 Outline

The presented method for the determination of 2D plasma parameters with filtered cameras observing the visible spectrum consists of three steps that are presented in this thesis.

In Ch. 2 the experimental setup and its calibration are described. The camera system at AUG was recently upgraded to measure the hydrogen Balmer α, β, and γ spectral lines simultaneously. Compared to other diagnostics the major advantage of filtered cameras is their high spatial resolution. An absolute calibration method for filtered cameras, presented in Sec. 2.2.3, has been advanced to reflect the more complex nature of optical inference filters in Sec. 2.2.4.

In Ch. 3 tomographic methods are applied to the images in order to reconstruct the toroidally symmetric distribution of visible light in 2D. Inverting camera images requires a forward model from emissions to image, Sec. 3.1. Realistic reflections are modeled as rough tungsten using detailed 3D construction drawings. To invert the forward model and reconstruct the distribution of emitted light, Bayesian statistics are employed in the framework of Gaussian process tomography. The reconstruction method is tested on simulated data and a technical low temperature plasma generated only by electron cyclotron resonance heating.

Finally, plasma parameters are inferred from these tomographic reconstructions in Ch. 4. This is possible using known photon emissivity coefficients for the hydrogen Balmer α, β, and γ spectral lines as a function of plasma parameters.

In Ch. 5 a first application to the X-Point radiator regime demonstrates the potential of filtered cameras to study the physics of a divertor plasma.

Chapter 2

Experimental Setup

The diagnostics used in the following chapters are described here. Section 2.2 is dedicated to filtered cameras.

2.1 ASDEX Upgrade

Dedicated experiments were carried out in the tokamak ASDEX Upgrade (**A**xially **S**ymmetric **D**ivertor **Ex**periment, AUG). As the name suggests, a central research field is divertor physics and the related power exhaust problem. Outstanding features of AUG are high available heating powers and plasma-facing components that are fully covered with tungsten. Further specifications and a sketch of the medium-sized tokamak can be found below.

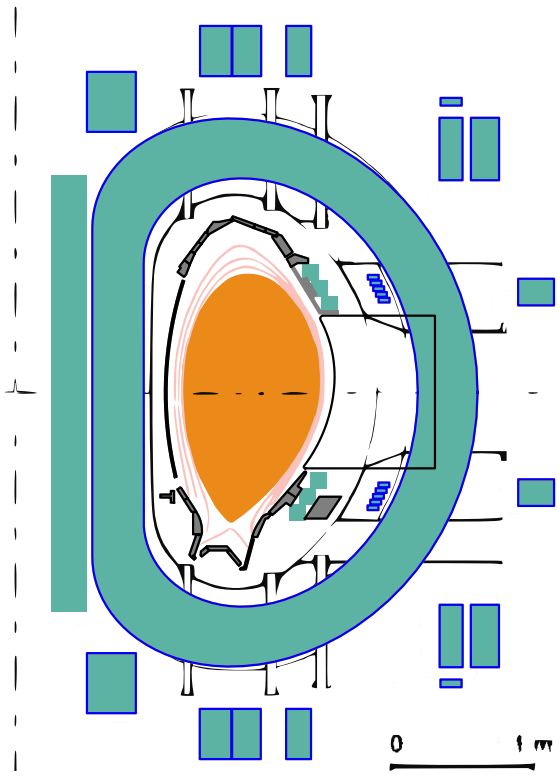

FIGURE 2.1: The AUG plasma (orange) is interacting with the first wall, which is mounted inside a vacuum vessel. Magnetic field coils (turquoise) are used to guide and shape the plasma.

Plasma heating	P_{heat}	< 27 MW
Toroidal field	B_t	< 3.1 T
Plasma current	I_p	0.4 - 1.5 MA
Pulse duration	t_{max}	< 10 s
Major plasma radius	R_0	1.65 m
Minor horizontal radius	a	0.5 m
Minor vertical radius	b	10.8 m
Triangularity	δ	0.4
Plasma volume	V	14 m^3
Plasma mass	m	3 mg

FIGURE 2.2: Specifications AUG. [11]

2.1.1 Divertor Thomson Scattering

Divertor Thomson scattering (DTS) is a new diagnostic in AUG to measure electron temperature and density in the divertor region. It allows for a direct and local measurement where in-situ measurement devices cannot be operated.

At the measurement position, laser light scatters elastically with free electrons, a process referred to as Thomson scattering[1]. Due to the Doppler shift the energy of a scattered photon depends on the velocity of the electron and the scattering angle. The spectrum of the scattered photons is broadened due the direction of the electron movement and can be analyzed to determine the electron temperature. The electron density is given by the intensity of the scattered photons.

The laser is pulsed, 50 ms are required to recharge it. Currently, 26 scattering volumes are measured along the laser beam, these are shown in Fig. 2.3 (a). For each scattering volume four spectral channels are available. Design values are $T_e = 1\,\mathrm{eV}$ to $100\,\mathrm{eV}$ for the electron temperature and $n_e = 10^{19}\,\mathrm{m}^{-3}$ to $10^{21}\,\mathrm{m}^{-3}$ for the electron density. At the limits of these intervals the signal to noise ratio decreases and data processing techniques need to be employed. [12, 13]

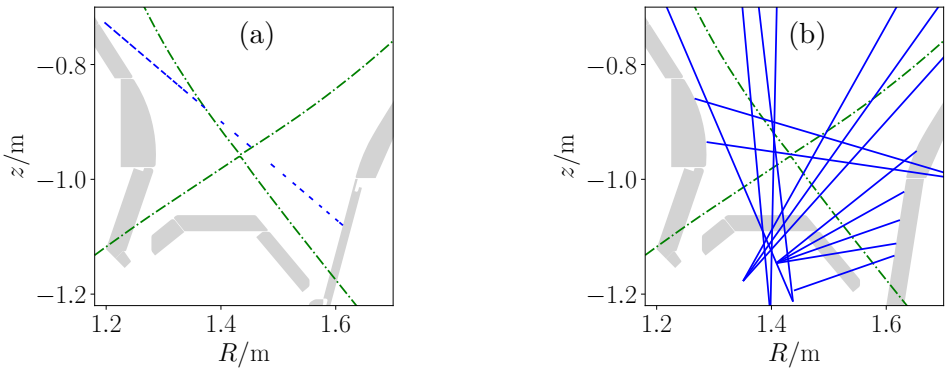

FIGURE 2.3: AUG divertor diagnostics: scattering volumes for DTS (a) and LoS for divertor spectroscopy (b). For orientation the separatrix of AUG discharge #38773@5.6 s (green, dash-dotted).

2.1.2 Divertor Spectroscopy

Line integrated plasma emissions can be measured quantitatively with divertor spectroscopy. The straight lines along which light is integrated are referred to as lines of sight (LoS). The integrated emissions are measured as radiance, see Sec. 3.1.1. Advantages of divertor spectroscopy are the high spectral resolution and absence of reflections. The latter is because the LoS end in the gap between tiles and enables a clean analysis. The high spectral resolution permits

[1]The low energy limit of Compton scattering, thus elastic.

two important features. First, a separate measurement of two spectral line emissions at a similar wavelength is possible. Second, even a spectral peak can be broken down into its components. This allows to analyze the Stark effect of electric fields or the Zeeman effect of magnetic fields, the Doppler broadening also needs to be considered. A method that allows for a determination of line integrated densities from Balmer emissions has been developed for the AUG divertor plasma. [14]

Some of the available divertor spectroscopy LoS in AUG are displayed in Fig. 2.3 (b).

2.2 Filtered Cameras

Line integrated plasma emissions can be measured quantitatively with filtered cameras. This quantity is referred to as radiance, see Sec. 3.1.1. The major advantage compared to divertor spectroscopy is the high spatial resolution. The number of LoS in the order of 10^5 makes it possible to apply tomographic techniques without the need of making strong assumptions on the emission pattern.

First, technical details for the used setups are given. Second, position and view of the cameras is determined from a line of sight calibration. Third, an absolute calibration is carried out to determine the proper units. At the end of this section improvements are introduced and it is shown how unexpected emissions can be identified.

2.2.1 Camera Setup

At AUG the spectral lines hydrogen Balmer α, β, γ and a nitrogen II multiplett can be measured simultaneously. The setup is shown in Fig. 2.4 and will be referred to as 06Bul-cameras. This name reflects the position of the camera in sector 6, see Fig. 2.5 (b), under the B-port on the left. To obtain an accurate and quantifiable spectral measurement, a modular setup with a spectral filter and a monochrome camera is used. Also the objective is modular; the aperture is adjustable and the objective lens can be exchanged. For the presented results, an objective lens with a focal length of 4 mm was used. The camera features a frame-rate of 120 Hz and an exposure time variable in 10 steps between 33 µs and 8.3 ms.

The 06Bul-cameras are particularly robust to withstand high magnetic fields and neutron exposure from the plasma. This allows for operation in close vicinity of the plasma. While this setup has a particularly high image quality, it is complemented by a filtered fast camera that is connected to the vessel via an image guide. This second setup has a frame-rate of about 10 kHz, at a reduced frame size up to 1 MHz are possible.

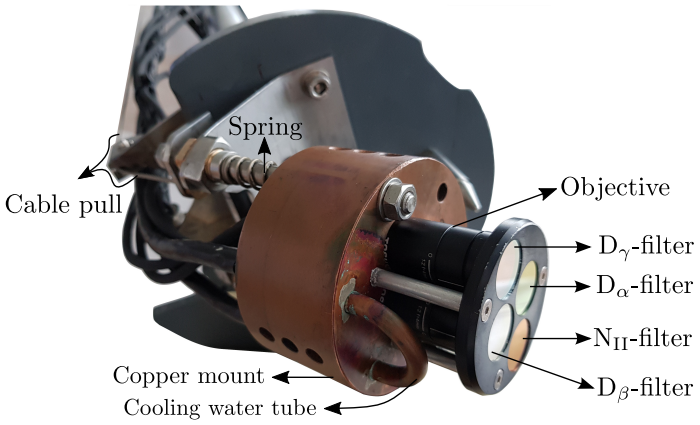

FIGURE 2.4: 06Bul-cameras, the main diagnostic used for this work. Modular setup consisting of a camera, an objective and a filter. Realized for the spectral lines hydrogen Balmer α, β, γ and a nitrogen II multiplett.

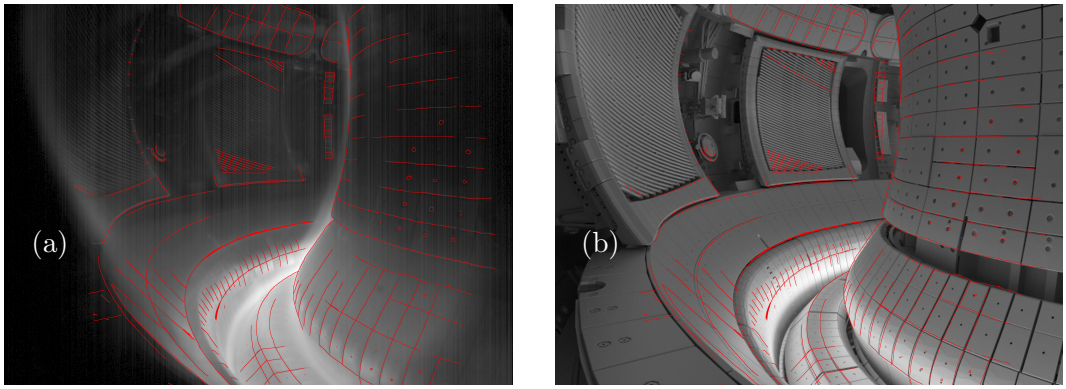

FIGURE 2.5: Identification of vessel contours in a measurement (a). The drawn contours (red) are placed in the CAD model (b).

2.2.2 Line of Sight Calibration

To apply tomographic techniques the viewing geometry has to be known with a high precision. The process of placing the cameras in the CAD geometry of the tokamak is sketched in the following. The four 06Bul-cameras have a similar view. However, their precise viewing direction differs by a few degrees and can even change between discharges, e.g. due to disruptions that can shake the whole machine. Aiming at a precision of 1 cm at a distance of 1 m requires an angular precision of $0.6°$. For the presented discharges this necessitated to repeat the calibration for each image.

First, characteristic contours have to be identified in the measured image. To minimize noise it is possible to combine images where the camera did not move, i.e. averaging over time. This has been done in Fig. 2.5 (a). To ease the placement in the CAD the characteristic contours are redrawn by hand (red). The identified contours are placed in the CAD by adjusting the camera view, which is defined by parameters such as camera position, viewing direction, dis-

tortion properties, etc. Starting with an approximate view, these parameters are modified until experimental contours and CAD match sufficiently well. A reasonable match is shown in Fig. 2.5 (b). The resulting camera view is defined by viewing directions for each pixel and the camera position. Neglecting the spatial extend of the camera optics is a good assumption for objects that are far away from the camera. However, such a pinhole model may introduce a small error when computing the angle of incidence for the filter. An alternative to the sketched workflow is to select characteristic point pairs in the CAD and the camera image to optimize the viewing geometry, this is e.g. implemented in the Calcam code [15].

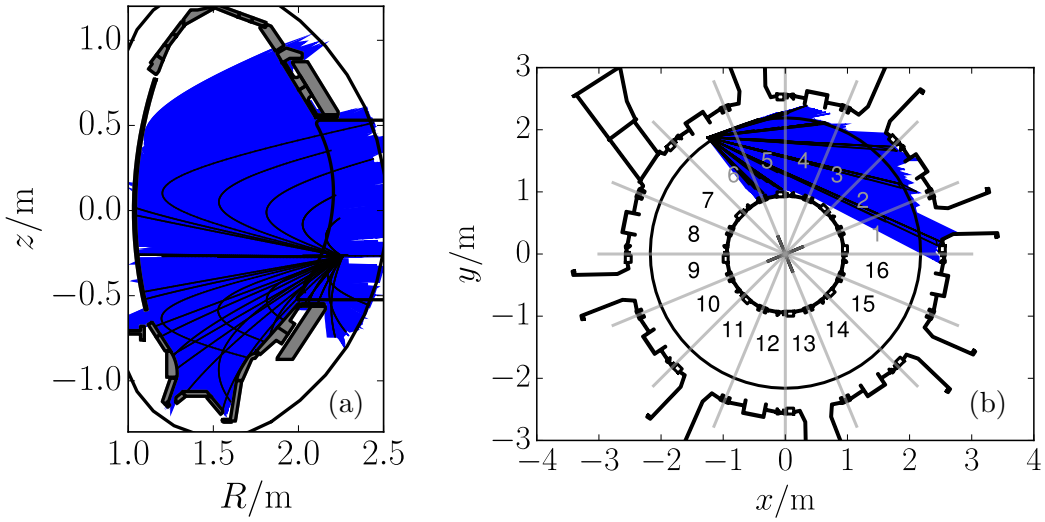

FIGURE 2.6: Field of view (blue) and every 100th LoS (black) for a 06Bul-camera in a poloidal (a) and toroidal (b) projection.

The camera position and the viewing direction for each pixel define a straight line, the term LoS refers to the line segment between the camera and the first intersection with the vessel structures. A poloidal and toroidal projection of every 100th LoS (black) is shown for a 06Bul-camera in Fig. 2.6, the LoS appear curved in the poloidal projection. All the LoS span the field of view (blue).

2.2.3 Absolute Intensity Calibration

In order to quantify the line integrated plasma emissions an absolute calibration is needed to obtain a relation between the camera raw data measured in counts Φ_{raw} and the radiance Φ. Radiance is the radiant flux incident on the camera, see Sec. 3.1.1 for further details. The relation is determined by the calibration constant C and the exposure time t_{exp}. An angle dependence will be introduced in the next subsection, but for now the relation reads $\Phi = C\Phi_{raw}/t_{exp}$. The calibration constant C can be determined with a source

of known radiance. A simple solution would be to use a calibrated deuterium discharge tube.

For this work black body radiation from halogen lamps is used. To get a homogeneous emitter, multiple halogen lamps are placed in an integrating sphere, also known as Ulbricht sphere. Its spectrum is given in Fig. 2.7 and is of interest within in the transmission window of the filter, here the D_α-filter. As a first approximation it is assumed that the filter transmits all photons with wavelength from 653 to 677 nm. Integrating the spectral radiance $\Phi(\lambda)$ over this wavelength interval yields the calibration value Φ_{calib}. In this first approximation the sphere is a D_α emitter with radiance Φ_{calib} and the calibration constant can be determined with a measurement of the sphere at some exposure time $C = \Phi_{calib}\, t_{exp}/\Phi_{raw}$.

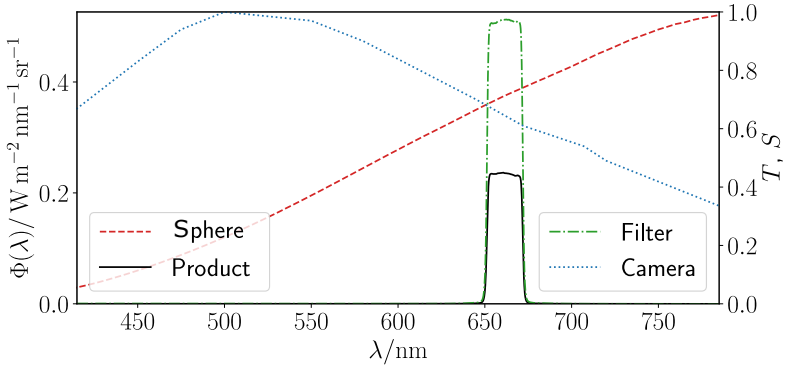

FIGURE 2.7: Spectral radiance $\Phi(\lambda)$ of the integrating sphere (red, dashed). Transmission T of D_α-filter for perpendicular incidence (green, dash-dotted). Camera sensitivity S (blue, dashed). Product of the three curves (black, solid).

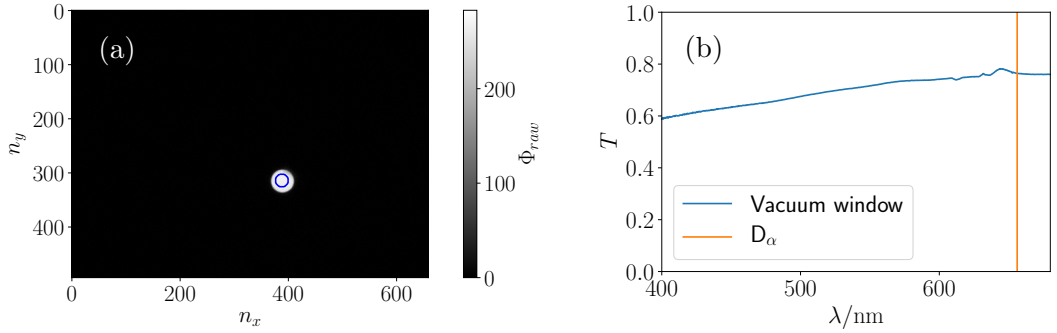

FIGURE 2.8: Calibration with an integrating sphere (a), used pixels are indicated by the blue circle. Calibrating outside the vessel necessitates considering the vacuum-window transmission (b).

For this calibration measurement it is important to use a camera sensor that was not yet exposed to neutron radiation. Even after a few days of deuterium plasma operation the cameras experience significant neutron damage.

This leads to an increase of the background[2] signal, especially at long exposure times. Long exposure times are required for calibration since the plasma is typically substantially brighter than the calibrated emitter. A different aperture is not a possible solution since this setting cannot be determined accurately.

Fig. 2.8 (a) shows a calibration image outside the vessel for the D_α-camera. The noise can be reduced by using the longest exposure time that does not lead to saturation and averaging over the blue circle. For the discharges in Ch. 5, the camera was exchanged within the campaign, making an in-vessel calibration impossible. To get a quasi in-vessel calibration, the images can be multiplied with the transmission of the vacuum window at the corresponding wavelength. This transmission was measured after the campaign using a spectrometer and a long optical fiber, the result in Fig. 2.8 (b) shows that the window blocks a significant fraction of the light.

It was assumed that the raw measurement is proportional to the exposure time, this requires that the camera precisely adapts this setting. For a confirmation the calibration can be conducted at various exposure times as in Fig. 2.9. Comparing to the fit of a line through the origin shows that the deviation from a linear dependency on the exposure time $\Phi_{raw} = mt_{exp}$ is negligible.

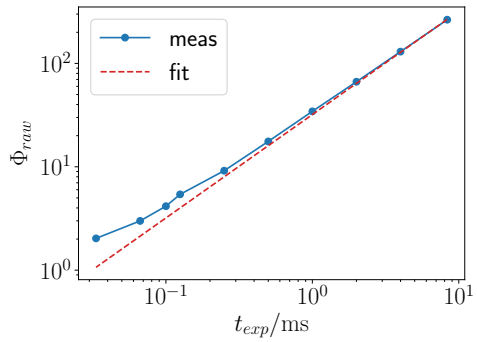

FIGURE 2.9: Result of calibration with D_α-camera for various exposure times (blue, solid with dots). Linear fit (red, dashed) with y-intercept preset to zero.

If the filter curve is not a rectangular function not only the spectral radiance of the sphere, but the product with the filter curve has to be integrated. If the desired plasma emissions are partially blocked by the filter, the integral needs to be divided by the transmission at the wavelength of the plasma emissions. The same applies if the sensitivity of the camera changes significantly over the transmission window of the filter. Such a product of filter curve, camera sensitivity and sphere radiance is shown in Fig. 2.7.

[2]The background is a measurement in absence of light and is used as a negative bias for the measurement.

2.2.4 Optical Inference Filters

Optical inference filters are used to obtain sharp transmission curves, their functional principle is explained in the appendix A. The transmission does not only depend on the wavelength, but also on the angle of incidence θ. The consequences for the camera diagnostic are discussed in the following.

The transmission of the D_α-filter at $\theta = 0°$ is displayed in Fig. 2.10 (a). It is the result of a spectroscopic measurement with light perpendicular to the filter. With the employed camera setup $\theta = 0°$ holds only in the center of the image, see contours of $\theta = 27°$ and $\theta = 29°$ in Fig. 2.10 (b).

For $\theta > 0°$ the filter curve is shifted towards the blue according to an analytic formula derived in the appendix A. This shift is given by a re-scaling of the wavelength by the scaling factor

$$\frac{\lambda_\theta}{\lambda} = \sqrt{1 - \frac{\sin^2 \theta}{n^2}}, \tag{2.1}$$

where $n \approx 2.05$ for the D_α-filter. Due to the filter shift the D_α transmission is strongly reduced between $\theta = 27°$ and $\theta = 29°$, see Fig. 2.10 (a). This filter effect is the reason why no significant radiation is received beyond an angle of 29° in Fig. 2.10 (b).

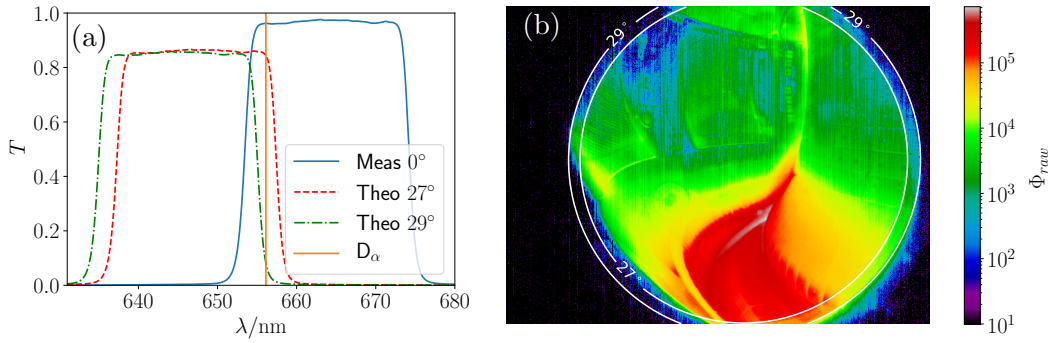

FIGURE 2.10: Transmission of the D_α-filter shows an angle dependence (a). Between $\theta = 27°$ and 29° the filter starts to block D_α. Recording of the 06Bul-camera equipped with this filter in false color representation (b). Because the filter blocks D_α no significant radiation is received beyond an angle of 29°.

The angle dependence is also evident in a close-up of the integrating sphere opening shown in Fig. 2.11 (a). Some dust on the camera setup reduces the observed brightness up to 20 %, but it can be clearly seen that the measured raw signal depends on the angle of incidence, which is not evident if the filter is removed. The data is fitted to a fourth order polynomial (black) in Fig. 2.11 (b). The fit coincides well with the moving mean (red) if the fit weights counteract the increase of data points at increasing θ. It is shown in Fig. 2.12 (a) that the wavelength shift is not sufficient to explain this angle dependence. Assuming that the filter curve is additionally multiplied by a factor $(1 - m\theta)$

yields a good match with spectrometer measurements at various angles of incidence, see Fig. 2.13. The slope m is determined using close-up data from the integrating sphere up to $\theta = 16°$. Nevertheless, this linear degradation reproduces the spectroscopic measurement also at $\theta = 30°$. The non-linear degradation for larger θ in Fig. 2.12 (b) can be related to the decrease of filter width, this third effect is not considered for the calibration.

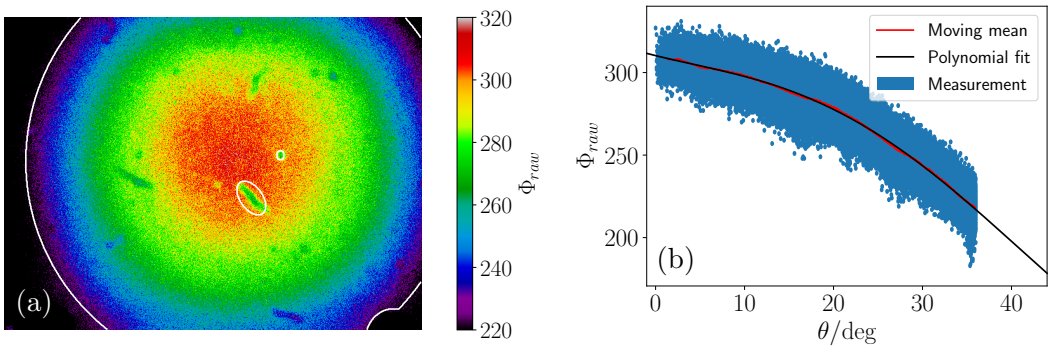

FIGURE 2.11: Close-up of the integrating sphere (a) and manually excluded regions (white, solid). The data reflects the filter dependence on the angle of incidence (b).

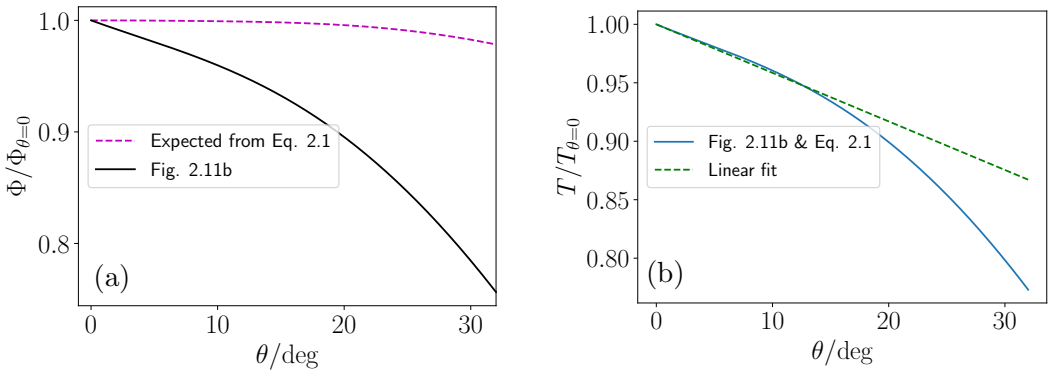

FIGURE 2.12: Filter dependence (black, solid) is not due to wavelength shift (a). Instead, the filter transmission degrades with angle of incidence (b).

2.2.5 Shifted center

While the $\theta = 29°$ contour touches the right border of the image in Fig. 2.10 (b), the left border is further away because the $\theta = 0$ LoS is not at the center of the image. While this might be explained with non-symmetric filter properties, such an effect could not be reproduced when examining the filter. A skew mounted filter would have been visible with shifts of up to 4°. Most of the shift could be attributed to a misalignment of the optical axis of the lens and the camera sensor. This is reasonable as every pixel has a width of 7.4 μm such that the misalignment is only 0.3 mm. For the close-up of the integrating

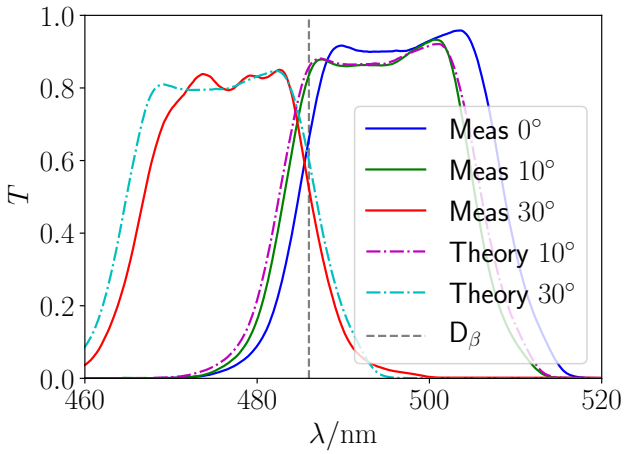

FIGURE 2.13: Linear degradation of filter transmission and wavelength shift describe spectrometer measurements for various θ precisely.

sphere, the center could be found in an automatized way, these values were slightly adapted for experimental data.

2.2.6 Relevance of Undesired Radiance

Neutrons generated by the plasma are impinging on the camera sensor and result in small bright spots on the image that can be removed with a median filter. Reflections are much more difficult to handle as they make a large part of the image. Even in an attempt to model reflections it is not feasible to represent every visible detail in the real world. For example, the heat loads in the divertor region have an effect on the reflectivity and lead to unevenly reflecting tiles. Furthermore, the camera setup can be seen as a reflection of the vacuum window in Fig. 2.14. The metal plate holding the circular filters in place can be seen because the springs, see Fig. 2.4, did not push the cameras close enough to the vacuum window.

Also one might observe undesired emissions from the plasma itself. This is evident in a recording with the D_γ filter shown in Fig. 2.15 (a). For this false color representation in log-scale many images of AUG discharge #38486 were summed up. Comparing to the filter transmission in Fig. 2.15 (b), the D_γ-line contributes only up to about 26°. While the counts do indeed decrease significantly, there are some emissions for larger angles of incidence. There is even a small band that is brighter than its surrounding around 33°. A plausible explanation would be that emissions from a N_I-multiplett and the D_δ-line are visible in this image.

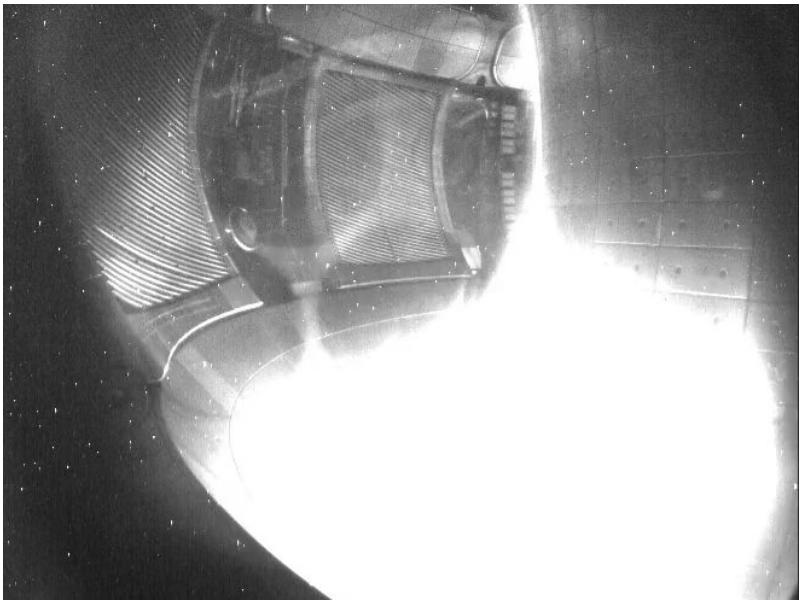

FIGURE 2.14: 06Bul-cameras see themselves as a reflection of the vacuum window.

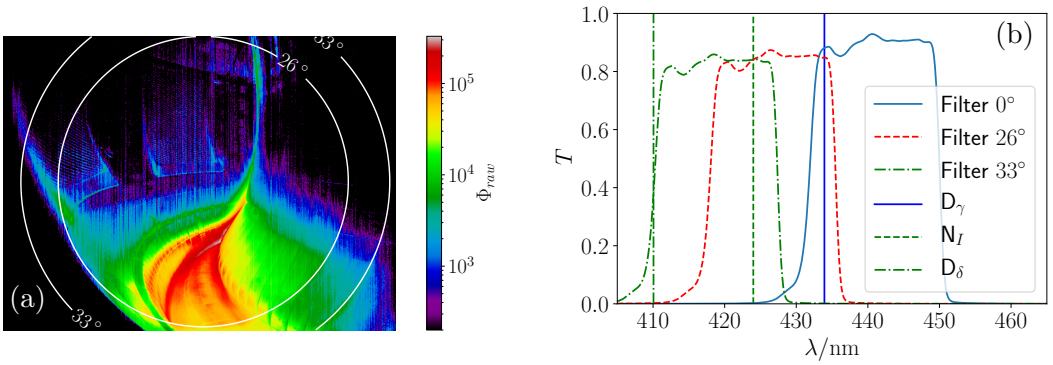

FIGURE 2.15: Undesired emissions from the plasma might be relevant. Recording with D_γ-filter (a) and filter transmission with relevant spectral lines (b).

Chapter 3

Emission Reconstruction

In this chapter the reconstruction of 2D emissions from camera images is explained in two sections. Fig. 3.1 gives a schematic overview of the calculations explained in this chapter. In Sec. 3.1 2D emission profiles are used to generate camera images in a forward model. A discretization of the forward model allows to invert the relation and reconstruct emissions from camera images. For the inversion, which is presented in Sec. 3.2, a tomographic method based on Bayesian probability theory is used in an innovative approach where photorealistic reflections can be modeled.

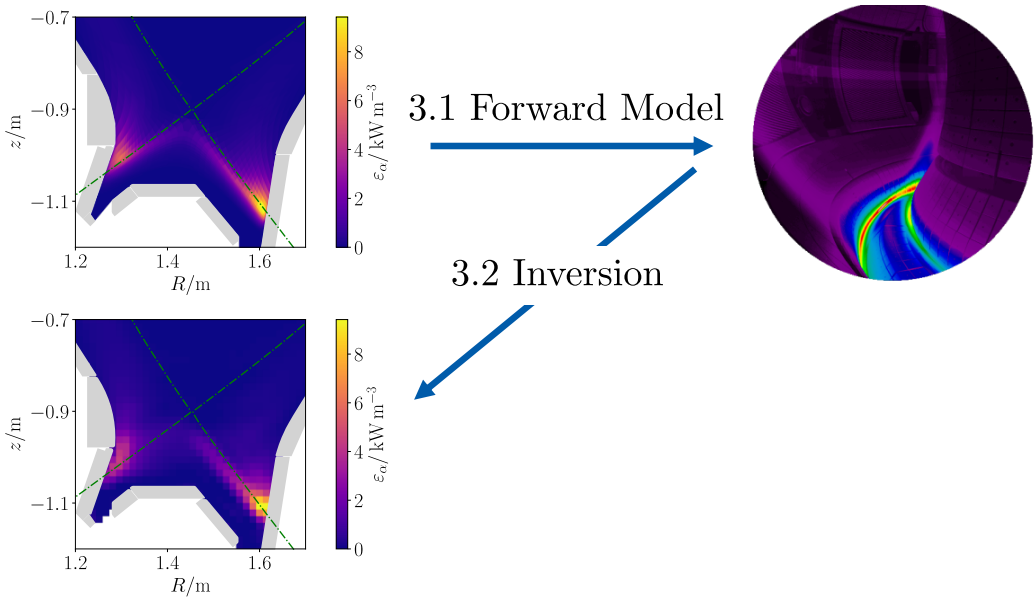

FIGURE 3.1: Overview for this chapter. The forward calculation of camera images from 2D emission profiles can be inverted using tomographic techniques.

3.1 Forward Model

This section describes the creation of images from 2D emissions. Volumetric emissions are line of sight (LoS) integrated to obtain an image, Sec. 3.1.1. The discretization is described in Sec. 3.1.2 allows for a computationally quick generation of an image. Finally, in Sec. 3.1.3 reflections from plasma facing components are added by ray tracing.

3.1.1 Line of Sight Integration

The camera view is defined by viewing directions for each pixel and the camera position, see Sec. 2.2.2. Together with a CAD model of the vessel this defines the LoS. For a light-absorbing vessel one can simply integrate plasma emissions along the LoS of each pixel.

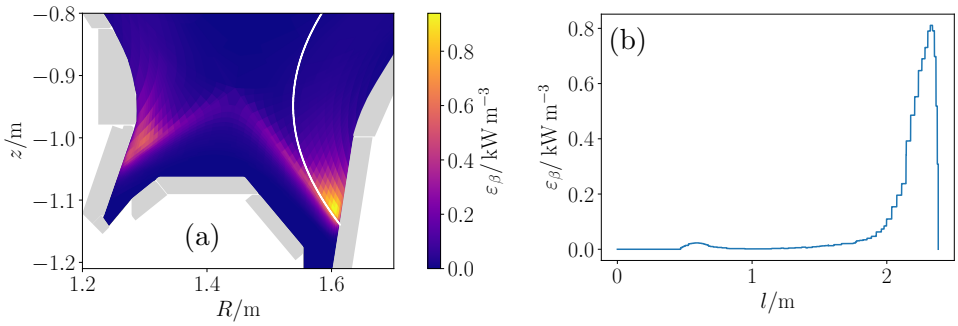

FIGURE 3.2: Poloidal projection of a LoS (white) on a sample emission pattern (a), the camera position is out of view. The emissions along the LoS (b) are integrated to obtain the brightness of the associated pixel.

Fig. 3.2 shows a poloidal projection of a straight LoS ending in the outer divertor leg (a) and the emissions seen along the LoS (b). More details on the emission profile are given in Sec. 4.4. Integrating (b) yields the brightness of the pixel associated to this LoS.

At first sight, the emissions further away from the camera should be scaled down, since the energy reaching the camera sensor decreases with distance squared. However, a camera pixel collects the light from a volume surrounding the LoS which can be approximated as a cone. The cross section of this cone increases with distance squared such that both effects cancel each other. A minor improvement of about $0.1 - 4\,\%$ can be obtained by volumetric sampling, i.e. integrating emissions within a cone limited by the LoS of the surrounding pixels. As long as an emitter is larger than the cone, the distance of an object does not influence its brightness.

The light collected by the sensor is also proportional to the effective area of the lens. From a technical point of view this effective area depends on focal length and aperture. To have a comparable unit, camera measurements are usually given per steradian of effective lens area seen from an emitter at unit distance. When simulating a camera image this introduces a division by

4π. The resulting calibrated camera measurement units are $\mathrm{Wm^{-2}sr^{-1}}$, this is referred to as radiance.

An exemplary image obtained from such a forward calculation is shown in Fig. 3.3. For this purpose the LoS in Fig. 2.6 were integrated along the emissions in Fig. 3.2 (b).

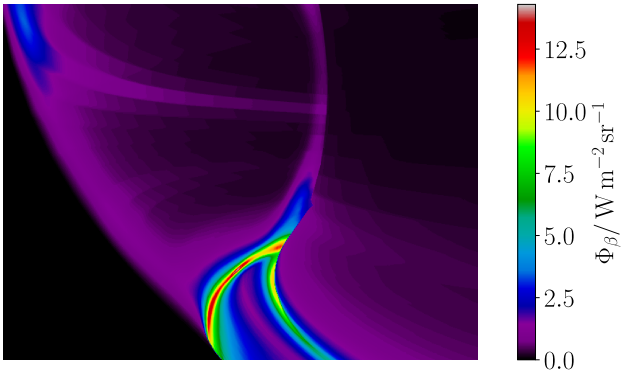

FIGURE 3.3: Artificial image for a 06Bul-camera without reflections. Therefore, each pixel is LoS integrated along the emissions.

3.1.2 Discretization

The LoS integration is possible for an arbitrary distribution of emitted light. For a fixed camera geometry it is possible to come up with a relation that allows for a computationally quick generation of camera images at a fixed discretization. For such a discrete forward model the world is split into grid cells that are referred to as voxel, changing the discretization is connected to computational effort. In this work, voxel are toroidally symmetric and in the poloidal plane they appear as equally sized squares with side length 14 mm, which is a good match with the feasible accuracy of the LoS calibration. To demonstrate the principle of a discrete forward model, the emissions in Fig. 3.2 (a) are averaged over each voxel. The resulting pattern in Fig. 3.4 can be represented by a matrix that can be assigned to a 1D vector $\vec{\varepsilon}$. Flattening also the matrix representing the image allows to come up with a matrix relation

$$\begin{pmatrix} \Phi_0 \\ \vdots \\ \Phi_{n_\Phi} \end{pmatrix} = \begin{bmatrix} S_{0,0} & \cdots & S_{0,n_\varepsilon} \\ \vdots & \ddots & \vdots \\ S_{n_\Phi,0} & \cdots & S_{n_\Phi,n_\varepsilon} \end{bmatrix} \begin{pmatrix} \varepsilon_0 \\ \vdots \\ \varepsilon_{n_\varepsilon} \end{pmatrix}, \tag{3.1}$$

where n_Φ is the number of pixel in the image and n_ε the number of voxel. In index notation $\Phi_i = \sum_j S_{i,j}\varepsilon_j$ it becomes clear that this discrete forward model represents an approximation of the LoS integration by a Riemann sum. The matrix S is referred to as sensitivity or geometric matrix and defines a linear map from emissions to image that is computationally quick. A row of

the sensitivity matrix S_j contains the length of the LoS within each voxel j, reflections can be added as well.

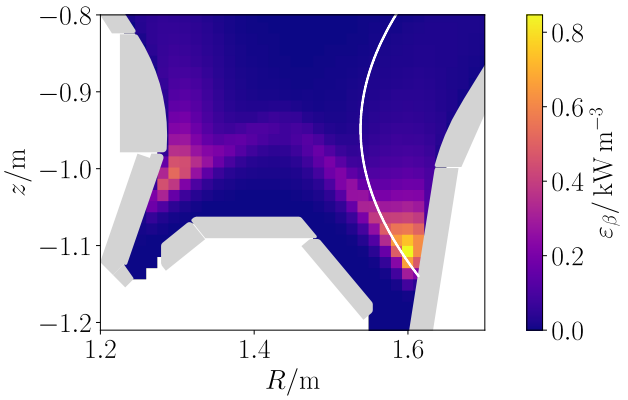

FIGURE 3.4: Emissions from Fig. 3.2 (a) re-sampled on the grid of the discrete forward model.

The L-norm will be used to obtain scalar measures for vector quantities. The L_2-norm is commonly known as the euclidean norm. The L_4-norm of a vector $\vec{x}$ is accordingly

$$||\vec{x}||_4 = \sqrt[4]{\sum_{i=1}^{n} |(\vec{x})_i|^4}, \tag{3.2}$$

where $(\vec{x})_i$ is an element of the vector $\vec{x}$ with length n.

The difference of an image obtained from the discrete and actual profile is a vector quantity $\Delta\vec{\Phi}$. A scalar measure for this discretization error is given by the relative L_4-norm difference $||\Delta\vec{\Phi}||_4/||\vec{\Phi}||_4$. For the previously described discretization it is 4.9 % when also modeling reflections. The relative L_2-norm difference, also referred to as normalized root mean squared error, is 3.0 %. Reconstructing a LoS integrated image with a discrete sensitivity matrix introduces a systematic deviation with a small kurtosis.

3.1.3 Reflections

The material of the plasma facing surfaces in AUG is tungsten. Camera measurements show reflections from these metallic surfaces. In accordance with Sec. 3.1.1 it does not matter how distant the emitting surface is. The observed radiance Φ_r of a reflective surface depends on material properties, the angle on which the LoS intersects this surface and the light that is incident on the surface. From the perspective of the surface incoming light Φ_i at a direction $\vec{\omega}_i$ is reflected in various outgoing directions $\vec{\omega}_o$. The light may be incoming from the hemisphere Ω at some angle of incidence $\theta(\vec{\omega}_i)$ w.r.t. the surface. In contrast to the previous approximation for the sensitivity of the camera with a curved lens, the radiance received by a flat surface needs to be multiplied with $\cos(\theta(\vec{\omega}_i))$. Arbitrary material properties can be described with a bidirectional

reflectance distribution function (BRDF) $f_r(\vec{\omega}_i, \vec{\omega}_o, \lambda)$. The reflected radiance of a surface can be calculated using

$$\Phi_r(\vec{\omega}_o) = \int_\Omega \Phi_i(\vec{\omega}_i) f_r(\vec{\omega}_i, \vec{\omega}_o) \cos(\theta(\vec{\omega}_i))\, d\vec{\omega}_i. \text{ [16]} \tag{3.3}$$

For specular reflection the integral collapses to a single direction $\vec{\omega}_i$ and the equation reads $\Phi_r = \Phi_i f_r$. For this case f_r is a constant reflectivity and is determined by the Fresnel equations. For ideal diffuse reflection an incoming light ray along $\vec{\omega}_i$ is evenly redistributed over the hemisphere. Both limits cannot represent the behavior of real tungsten accurately, instead it was proposed for "fusion relevant materials [to be] modeled with the Cook-Torrance BRDF, which was parameterized in terms of the Fresnel equations and the GGX micro-facet surface model (...)" [16]. Those "micro-facets reflect specularly" and the "micro-facet redistribution model (...) includes self-shadowing, internal reflections, and absorption". [16]

For this work reflections were modeled with the CHERAB framework [17] that features a material library for rough tungsten. The sample size for the Monte-Carlo integration of Eq. 3.3 was selected such that a noise level $< 1\%$ is achieved. It is in the order of 10^4 for every of the about 10^5 camera pixels. The ray-tracing is even continued for the incoming radiance Φ_i, thus multiple reflections are considered. Fig. 3.5 (a) shows the result of adding reflections from detailed 3D construction drawings to the image in Fig. 3.3. The difference of both images, i.e. the bare reflections, are shown in Fig. 3.5 (b). Reflections are less relevant if the emissions are further away from the wall. The ratio of the L_2-norm of both images, i.e. the relative L_2-norm difference of the reflections, is 28 %. The relative L_4-norm difference is only 24 %. The systematic deviation that would be introduced when not modeling these reflections has a small kurtosis since reflections do not strongly affect regions of high radiance.

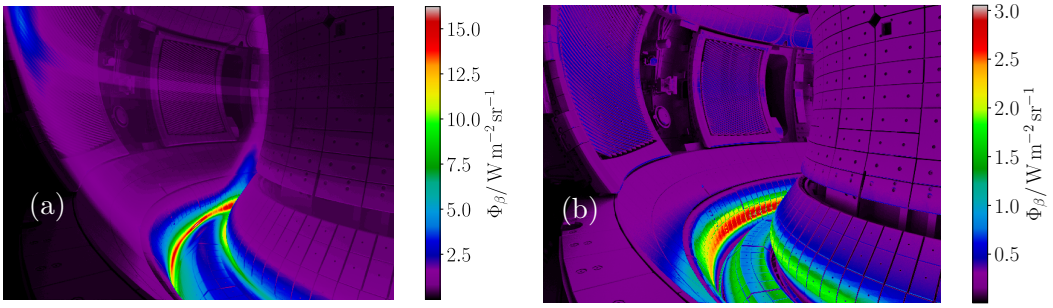

FIGURE 3.5: Adding reflections to the image (a). Difference of image with and without reflections (b), i.e. the bare reflections.

3.2 Inversion

The inverse problem of inferring 2D emissions from an image $\vec{\varepsilon} = S^{-1}\vec{\Phi}$ is discussed in this section. It is stressed that S^{-1} is a pseudo-inverse because the

sensitivity matrix is not a square matrix and the problem is not necessarily determined. Reconstructions considering a realistic and detailed reflection model are challenging, but have been successfully conducted [16, 18]. An innovative approach using Gaussian process tomography (GPT) is presented in the following. First, the assumptions and the method are introduced. Subsequently the tomographic method is tested against simulated camera images. Third, an application to first experimental data is shown.

3.2.1 Gaussian Process Tomography

GPT was presented for the first time in [19] and has been used with other AUG diagnostics [20]. A more comprehensive introduction is given in [21].

The employed GPT is based on two probability distributions, likelihood and prior. The measurement $\vec{\Phi}$ and its assumed uncertainty $\vec{\sigma_\Phi}$ define the likelihood $p(\vec{\Phi}|\vec{\varepsilon})$, a measure of how well a certain solution $\vec{\varepsilon}$ matches the image $\vec{\Phi}$. The uncertainty $\vec{\sigma}_\Phi$ is measured as a standard deviation and is constant for all pixels of the image σ_Φ in this work. A more complex assumption could not yield better results so far. The prior $p(\vec{\varepsilon})$ is defined by the covariance matrix Σ_ε and serves as a regularization of the result $\vec{\varepsilon}$ to punish large gradients between adjacent voxels. The squared exponential

$$(\Sigma_\varepsilon)_{i,j} = \sigma_\varepsilon^2 \exp -\frac{(\vec{r_i} - \vec{r_j})^2}{2l^2} \tag{3.4}$$

is used for the regularization, where $(\vec{r_i} - \vec{r_j})^2$ is the squared euclidean distance of two voxel. The regularization is constant throughout the poloidal plane and determined by the two scalars correlation factor σ_ε and correlation length l.

The probability of a certain emission profile given the measured image is denoted with $p(\vec{\varepsilon}|\vec{\Phi})$. The maximum of this posterior distribution defines the solution $\vec{\varepsilon}_{GPT}$. The distribution can be related to known quantities using Bayes' theorem

$$p(\vec{\varepsilon}|\vec{\Phi}) = p(\vec{\varepsilon})\frac{p(\vec{\Phi}|\vec{\varepsilon})}{p(\vec{\Phi})}. \tag{3.5}$$

The posterior is proportional to the prior $p(\vec{\varepsilon})$ and likelihood $p(\vec{\Phi}|\vec{\varepsilon})$ of the emission profile. Additionally, there is a normalization by the probability of the measurement $p(\vec{\Phi})$ that has not yet been introduced, it is constant and its covariance matrix is $\Sigma_\phi = \mathbb{1}\sigma_\phi^2$. To find the solution one could try many emissions $\vec{\varepsilon}$ and use the most probable one. However, an implementation of this search is probably not very elegant or computationally not achievable.

Instead, it is assumed that the solution can be written as a linear map $\vec{\varepsilon} = S^{-1}\vec{\Phi}$ and that all probabilities follow a multivariate Gaussian distribution. The linear map allows to propagate the error of the image to the posterior

$$\Sigma_{\varepsilon|\Phi} = S^{-1}\Sigma_\Phi(S^{-1})^T = S^{-1}\sigma_\Phi^2(S^T)^{-1}. \tag{3.6}$$

The posterior covariance matrix is part of the solution, thus rewriting this equation yields the inverse sensitivity matrix

$$S^{-1} = \Sigma_{\varepsilon|\Phi} \frac{S^T}{\sigma_\Phi^2}. \tag{3.7}$$

$((S^T)^{-1})^{-1} = S^T$ is an approximation reflecting that reconstructed emissions construct the input image.

The posterior covariance matrix can be obtained using Eq. 3.5. When multiplying probability distributions the resulting covariance matrix can be calculated as

$$\Sigma_{\varepsilon|\Phi} = (\Sigma_\varepsilon^{-1} + \Sigma_{comb}^{-1})^{-1}, \tag{3.8}$$

where Σ_{comb} is the covariance of $p(\vec{\Phi}|\vec{\varepsilon})/p(\vec{\Phi})$. Expanding this fraction by using the definitions for a multivariate Gaussian distribution allows to complete squares which yields

$$\Sigma_{comb}^{-1} = S^T \Sigma_\Phi^{-1} S = S^T S/\sigma_\Phi^2. \tag{3.9}$$

Having an explicit formula for the posterior covariance

$$\Sigma_{\varepsilon|\Phi} = (\Sigma_\varepsilon^{-1} + S^T S/\sigma_\Phi^2)^{-1} \tag{3.10}$$

allows for the determination of a pseudo inverse with Eq. 3.7. The inverse is defined by the sensitivity matrix S and three scalars: the uncertainty of the measurement σ_Φ, the correlation length l and the correlation factor σ_ε.

3.2.2 Optimization of Hyper-parameters

Correlation factor and length are referred to as hyper-parameters $\vec{\theta} = (\sigma_\varepsilon, l)$. Instead of using arbitrary values, their probability is optimized for the measurement $p(\vec{\theta}|\vec{\Phi})$. Using the most probable hyper-parameters and disregarding the uncertainty of the distribution $p(\vec{\theta}|\vec{\Phi})$ leads to an overconfident posterior emission, but the effect is small for two scalar hyperparameters. Before the prior served as a regularization, now $p(\vec{\theta})$ is constant such that Bayes' theorem reads

$$p(\vec{\theta}|\vec{\Phi}) = p(\vec{\theta}) \frac{p(\vec{\Phi}|\vec{\theta})}{p(\vec{\Phi})} \propto p(\vec{\Phi}|\vec{\theta}). \tag{3.11}$$

It can be derived that

$$-\ln(p(\vec{\Phi}|\vec{\theta})) \propto \ln(\det(M)) + \vec{\Phi} M^{-1} \vec{\Phi}, \tag{3.12}$$

where

$$M = S \Sigma_\varepsilon S^T + \Sigma_\Phi, \tag{3.13}$$

see Appendix C of [20].

The Nelder-Mead algorithm, implemented in the SciPy library [22], proved to minimize this function reliably w.r.t. the hyperparameters, this has also

been reported in [20]. In contrast to $p(\varepsilon|\Phi)$, the optimization of $p(\Phi|\theta)$ is computationally affordable since only two scalars have to be varied. However, the speed of a single evaluation strongly depends on the size of the matrices. When inverting visible camera measurements the optimization of σ_ε and θ_l introduces the need for high performance computing.

3.2.3 Estimation of Measurement Uncertainty

The GPT necessitates an estimation of the measurement uncertainty, but it is not sufficient to determine the noise level. For example, the sensitivity matrix may not describe observed reflections perfectly. Even for the artificial image σ_Φ needs to be significantly larger than zero because of the discretization. While it is difficult to approximate such systematic errors a priori, σ_Φ can be optimized on the precision of the tomographic reconstruction.

Therefore, the inverse will be evaluated for many different σ_Φ (optimizing the hyper-parameters each time) and applied to the image. The reconstructed emissions are then forward modeled and compared to the input data, this comparison is referred to as retrofit. The retrofit precision is measured with $||\Delta\vec{\Phi}||_4/||\vec{\Phi}||_4$ here. Even though optimizing the 2-norm yielded marginally better emissions for the artificial image, for experimental data the fit was visibly better when optimizing the 4-norm. This unusual approach is motivated by the lacking accuracy of the forward model in terms of reflections. In contrast to the systematic error introduced by the discretization, reflections have a small kurtosis. To set the focus away from the lacking accuracy of the reflection model, but rather improve on the few bright pixels showing the actual emissions, the 4-norm is optimized.

3.2.4 Testing with Simulated Data

In this subsection GPT is applied to the artificial camera images, using e.g. the simulation of a partially detached L-mode shown in Fig. 3.5 (a). The reconstructed emissions cannot fit the image perfectly because of the finite poloidal resolution of the sensitivity matrix. When generating the image with the sensitivity matrix the inversion is a mathematical problem and the emissions can be reconstructed precisely. For this problem it was not even necessary to use advanced tomographic methods, the pseudo-inverse provided by the numpy library [22] (Moore-Penrose inverse) achieved floating point accuracy inversions. However, this inverse produced strong artifacts when applied to the line integrated image. To reduce the computational effort with GPT, each four neighboring pixels are averaged. Because of filter shifts in the experimental image only LoS up to $\theta = 27°$ are included.

There is almost no noise for artificial camera images; however, due to the discretization the uncertainty is significant. The optimized value is $\sigma_\Phi = 0.04\,\mathrm{Wm^{-2}sr^{-1}}$ for the L-mode simulation. In order to relate this to the bright-

ness of the 2D image, the average L_4-norm is defined here as

$$||\vec{x}||_{\overline{4}} = \sqrt[4]{\frac{1}{n}\sum_{i=1}^{n}|(\vec{x})_i|^4}, \tag{3.14}$$

where $(\vec{x})_i$ is an element of the vector $\vec{x}$ with length n. Table 3.1 lists the relative measurement error, hyperparameters and the retrofit precision for various input images. The retrofit precision is $||\Delta\vec{\Phi}||_4/||\vec{\Phi}||_4 = 2.7$ % for the L-mode simulation. The full retrofit, i.e. the difference of input and reconstructed image, is displayed in Fig. 3.6.

Input image	$\sigma_\Phi/\,||\vec{\Phi}||_{\overline{4}}$	$\theta_l/\,\mathrm{mm}$	$\theta_\sigma/||\vec{\varepsilon}_{GPT}||_{\overline{4}}$	$\theta_\sigma/||\vec{\varepsilon}_{GPT}||_\infty$	$||\Delta\vec{\Phi}||_4/||\vec{\Phi}||_4$
Simulation L-mode	1.2 %	22	30 %	4.2 %	2.7 %
#39142 ECRH	20 %	1.1	66 %	12 %	11 %
D_γ of #38773	25.4 %	0.53	61 %	9.5 %	12 %
Simulation #38486	36 %	11	23 %	2.2 %	19 %
#38773 (1.8 T)	37 %	0.24	73 %	9.5 %	17 %
#38486 (2.5 T)	38 %	0.28	81 %	15 %	20 %

TABLE 3.1: Values of important GPT parameters determined for various input images. These are two artificial images from simulation and otherwise experimental data from AUG.

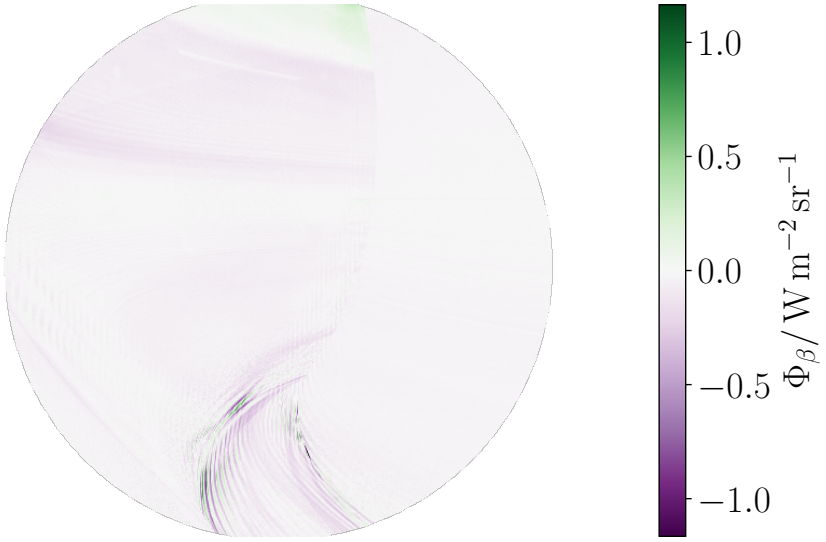

FIGURE 3.6: Difference of input and reconstructed image $\vec{\Phi}-\vec{\Phi}_{GPT}$ for a simulation of a partially detached L-mode.

For an artificial image also reconstructed emissions $\vec{\varepsilon}_{GPT}$ can be compared to the input emissions $\vec{\varepsilon}$ from the simulation. The volumetric integral of the

input emissions $P_\beta = 136$ W compares well to the integral of the reconstruction $P_{\beta,GPT} = 139$ W. A 2D difference to the resampled emissions[1] from Fig. 3.4 is shown in Fig. 3.7 (a). The relative L_2-norm of this emission retrofit is 34 %, it can be seen that emissions close to the wall are shifted even further towards it. Another type of artifact can be seen when reconstructing the emissions of an XPR simulation, see Fig. 3.7 (b). These elongated artifacts appear because a single SOLPS grid cell emits most of the light and the tomographic grid does not fit very well to this. Since they are barely visible on the image retrofit, it is difficult to identify such artifacts in experimental reconstructions.

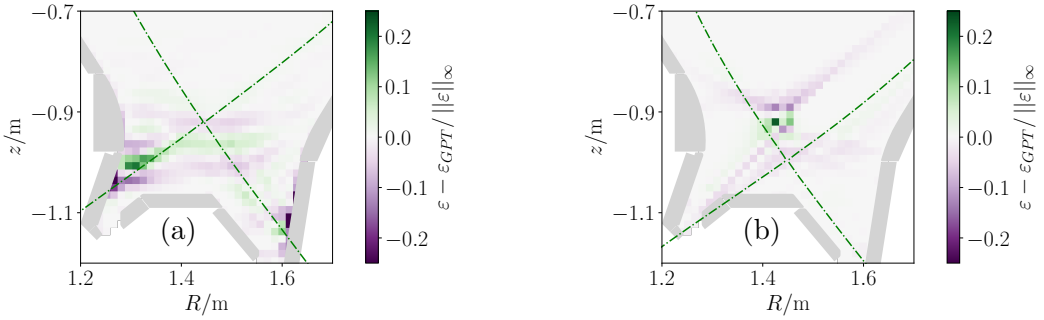

FIGURE 3.7: GPT on first simulated camera images. Difference of actual and reconstructed emissions $\vec{\varepsilon} - \vec{\varepsilon}_{GPT}$. Reconstructing emissions close to the wall is particularly difficult (a). Minor artifacts appear e.g. due to an insufficient resolution of the tomographic grid (b).

The GPT also yields 2D uncertainties for the emission pattern (the diagonal of the posterior covariance matrix $\Sigma_{\varepsilon|\Phi}$). This can be compared to the actual difference in emissions $\Delta\vec{\varepsilon} = \vec{\varepsilon}_{GPT} - \vec{\varepsilon}$. Their ratio is in the order of 1 for most voxel, values of 60 are reached as well. This may be attributed to the large kurtosis introduced by the discretization, which is significantly higher than the kurtosis of Gaussian noise.

3.2.5 Testing with Experimental Data: ECRH Generated Plasmas

Fig. 3.8 (a) shows a camera image of a plasma generated only by electron cyclotron resonance heating (ECRH). These plasma are used for wall conditioning and cleaning purposes if present magnetic fields do not allow for glow discharges. This will be required during the operational campaign of the ITER tokamak since the superconducting cannot be switched off. For this technical low temperature plasma no plasma current is induced and only electron cyclotron heating is applied. The photons are reflected on the metallic walls until they are eventually absorbed by the plasma, resulting in the plasma emissions observed by the cameras. A close-up of the reconstructed emissions in

[1] A bi-linear interpolation of the reconstructed emissions allows for a comparison to the high resolution profile, this results in a slightly larger L_2-norm difference of 36 %.

Fig. 3.8 (b) shows elongated emissions towards the camera position at $R > 1.8$ m. This small artifact illustrates that at the border of the viewed area, where the LoS are mostly parallel, the camera image conveys too little information. The aperture used during the measurement was not ideal for these experiments where the overall brightness of the plasma is small, resulting in a high Gaussian noise level. However, the retrofit precision of 11 % is the best value among experimental data and the reconstructed image in Fig. 3.8 (c) looks very similar to the input. The tomographic reconstruction worked so well due to the particular emission pattern where the emitted light is far away from the wall. Therefore, the emissions can be observed on many different LoS and reflections are less important.

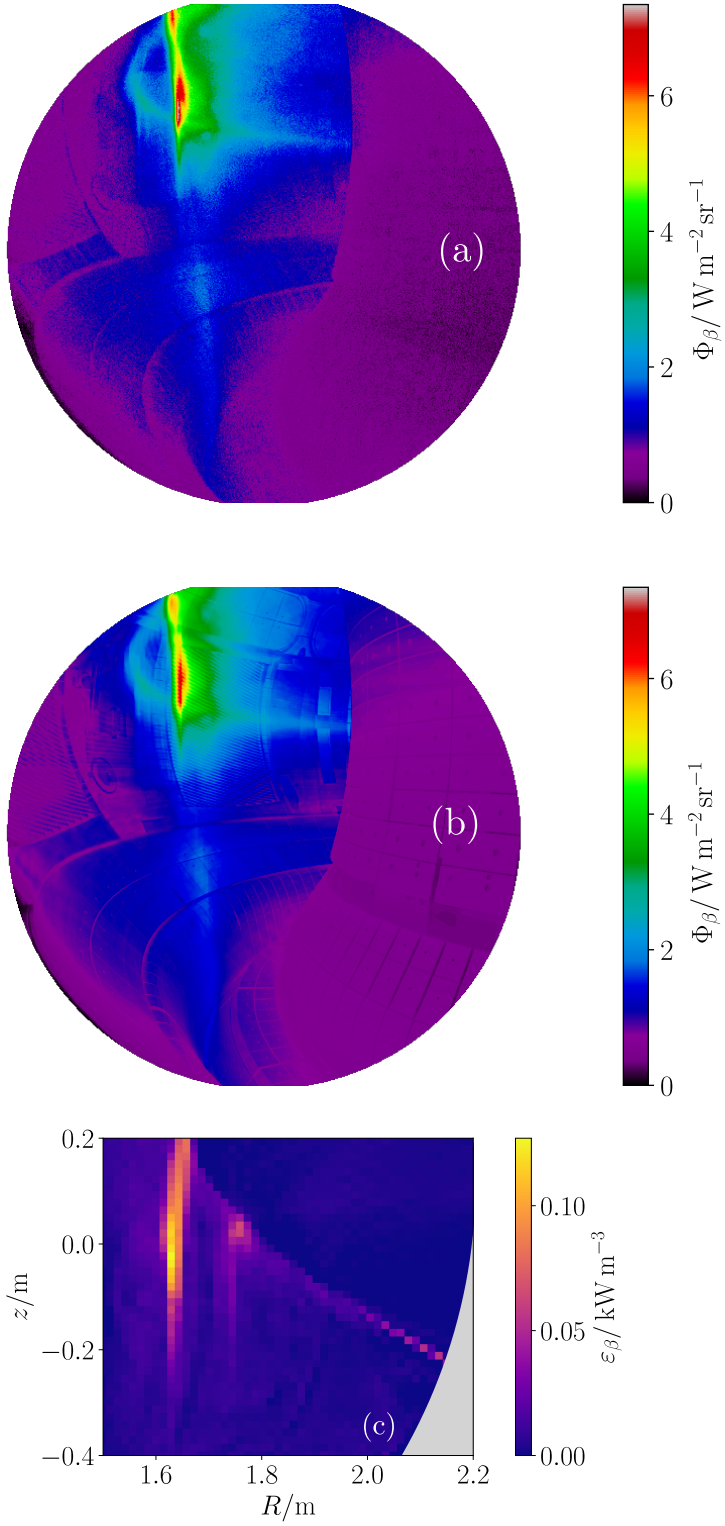

FIGURE 3.8: Emission reconstruction for AUG "discharge" #39142@0.47s, a plasma generated only by electron cyclotron resonance heating. Using the measured image (a) the distribution of emitted light $\vec{\varepsilon}_{GPT}$ (c) can be reconstructed. The reconstruction can be forward modeled $\vec{\Phi}_{GPT} = S\,\vec{\varepsilon}_{GPT}$ (b) and appears very similar to the measurement for the human eye.

Chapter 4

Inference of Plasma Parameters

The determined hydrogen Balmer α, β and γ emissions at some position in the poloidal plane can be used to infer electron temperature and density as well as neutral density, which is referred to as inference of plasma parameters. However, the inferred range of possible parameters can be large. The determination of emissions for known parameters is described in Sec. 4.1. This relation is used to infer plasma parameters in Sec. 4.2. Probabilities are introduced with Bayesian inference in Sec. 4.3. The first three sections serve as a basis to discuss and test the method for the determination of 2D plasma parameters with filtered cameras on a simulation of a partially detached L-mode in Sec. 4.4. Application to first experimental data is shown in Sec. 4.5.

4.1 Determination of Emissions from Plasma Parameters

The electron of an excited hydrogen atom may relax to the second lowest energy level, leading to the emission of a photon in the Balmer series. The number of emitted photons per unit time and volume is denoted by ϵ. For example, ϵ_α depends on the density of hydrogen atoms excited to the third lowest energy level where the electron has principal quantum number three. In a local thermal equilibrium the population of excited states is distributed according to a Boltzmann distribution. However, this holds only if an excited hydrogen atom undergoes many collisions such that the energy is distributed before the radiative process sets in. In a coronal picture the timescale of the radiative process is small compared to the collisions. At the plasma condition analyzed in this work, a description beyond this picture is needed since densities are too high to neglect collisions of excited hydrogen. However, densities are too low to justify a Boltzmann distribution. Therefore, excitation processes are studied in a generalized collisional-radiative model.

The dominant excitation processes are electron impact excitation of a neutral hydrogen atom and recombination of a proton with an electron. Charge exchange of a proton and a neutral can be disregarded as an additional emission

source because of a low cross section. The break-up of a deuterium molecule by electron impact leads to such emission, but plasma-molecule interactions are neglected in this work. The recombination emissions scale with the squared density n_e^2 since ion and electron densities are assumed to be equivalent. The excitation emissions are proportional to the electron density n_e and neutral density n_0. The generalized collisional-radiative modeling results in a photon emissivity coefficient $PEC(n_e, T_e)$. The emissions for a specific transition (i.e. D_α, D_β or D_γ line) are consequently

$$\epsilon = n_e n_0 PEC_{ex}(n_e, T_e) + n_e^2 PEC_{rec}(n_e, T_e). \tag{4.1}$$

In order to obtain the emitted power ε, Eq. 4.1 needs to be multiplied by the photon energy E_{ph}

$$\varepsilon = \epsilon E_{ph} = \epsilon \frac{hc}{\lambda}, \tag{4.2}$$

where h is the Plank constant, c the speed of light and λ the wavelength of the regarded spectral line.

The results of the modeling for hydrogen Balmer β, obtained from the ADAS database [23], are shown in Fig. 4.1. The photon emissivity coefficient for recombination (a) decreases with temperature. The excitation coefficient (b) increases approximately up to the ionization energy of hydrogen (14 eV).

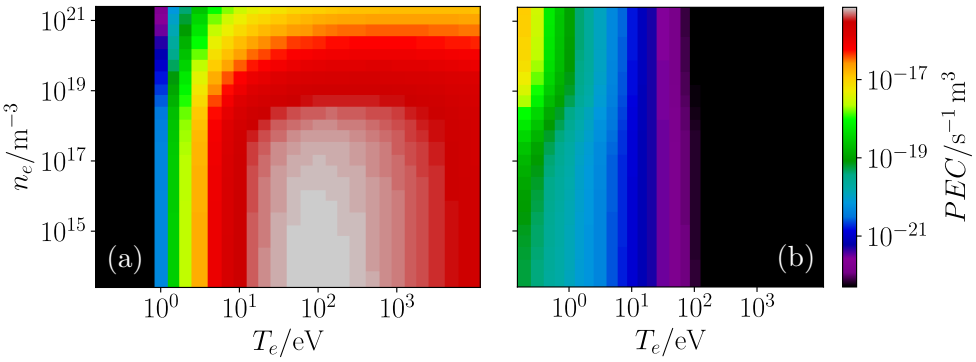

FIGURE 4.1: Photon emissivity coefficient for hydrogen Balmer β at according to the atomic and molecular database ADAS [23] for excitation (a) and recombination (b).

The hydrogen Balmer emissions depend on three quantities, which is difficult to visualize. Using a fixed neutral density $n_0 = 1.0 \times 10^{19}\,\mathrm{m}^{-3}$ D_β emissions are illustrated in Fig. 4.2 in terms of magnitude and relative amount of recombination.

4.2 Inference of Plasma Parameters from Hydrogen Balmer Emissions

Emissions can be calculated from plasma parameters, the plasma parameters $n_e = 1 \times 10^{19}\,\mathrm{m}^{-3}$, $n_0 = 1 \times 10^{19}\,\mathrm{m}^{-3}$ and $T_e = 4$ eV shall serve as an example.

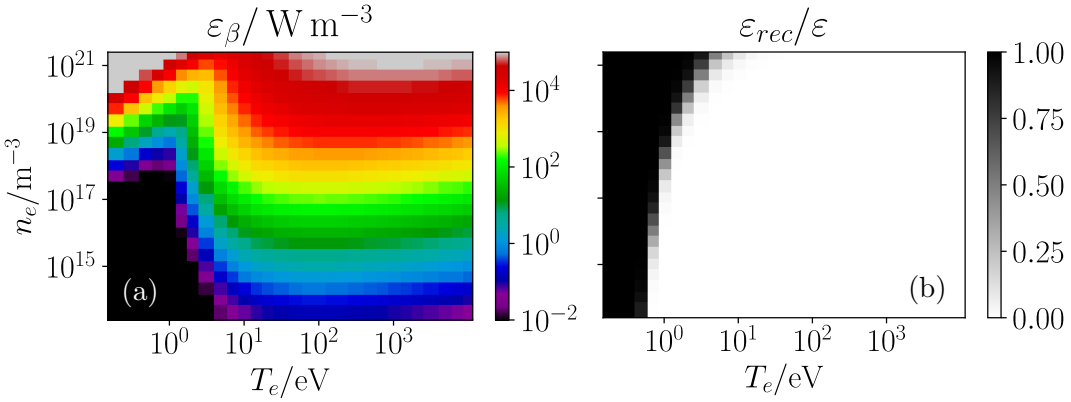

FIGURE 4.2: Magnitude (a) and fraction of recombination (b) of hydrogen Balmer D_β emissions for $n_0 = 1.0 \times 10^{19}\,\mathrm{m}^{-3}$.

Using Eq. 4.1 yields the according Balmer emissions $\varepsilon_\alpha = 4.5\,\mathrm{kWm}^{-3}$, $\varepsilon_\beta = 0.66\,\mathrm{kWm}^{-3}$ and $\varepsilon_\gamma = 0.11\,\mathrm{kWm}^{-3}$. These emissions cannot be inserted into an explicit equation to obtain the plasma parameters, instead a possible range of plasma parameters is inferred. Therefore, it is assumed that the emissions are not known precisely, but within a range of $\pm 30\,\%$.

Fig. 4.3 shows a basic inference given that the neutral density is known. The principle for a single line is shown on the left. The electron density and temperature that allow for $\varepsilon_\beta = 0.66\,\mathrm{kWm}^{-3}$ are shown by the solid contour. The dashed contours are the upper and lower limits for the range of $\pm 30\,\%$. The dashed contours limit possible plasma parameters to the green area shown on the right. Also D_α (red) and D_γ (blue) limit the parametric range further. The intersection of the three areas is shown in black and represents the range of possible plasma parameters. If the emissions are known precisely the range narrows down quickly until three lines cross in one point.

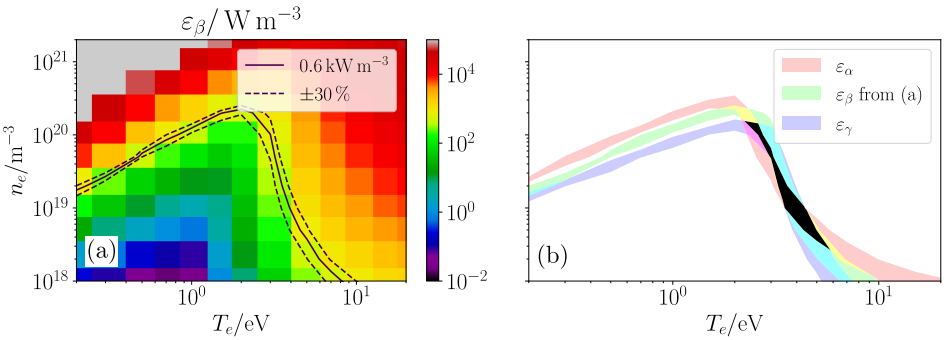

FIGURE 4.3: Inference of electron density and temperature for $n_0 = 1.0 \times 10^{19}\,\mathrm{m}^{-3}$ using $\varepsilon_\alpha = 4.5\,\mathrm{kWm}^{-3}$, $\varepsilon_\beta = 0.66\,\mathrm{kWm}^{-3}$ and $\varepsilon_\gamma = 0.11\,\mathrm{kWm}^{-3}$ within a range of $\pm 30\,\%$. The emissions from Fig. 4.2 are shown in (a) as well as the contour of the ε_β measurement. The dashed lines represent the upper $+30\,\%$ and lower $-30\,\%$ margin and define the green area in (b). Intersecting with the areas of ε_α and ε_γ limits possible electron density and temperature to the black area.

Fig. 4.4 shows that the three contours do cross in a single point for the correct neutral density, but not for $n_0 = 1.5 \times 10^{18}\,\mathrm{m}^{-3}$. However, emissions would have to be known within a range of about 1 % to exclude $n_0 = 1.5 \times 10^{18}\,\mathrm{m}^{-3}$. With reasonable error bars it is not possible to determine all three plasma parameters using no further assumptions than ε_α, ε_β and ε_γ.

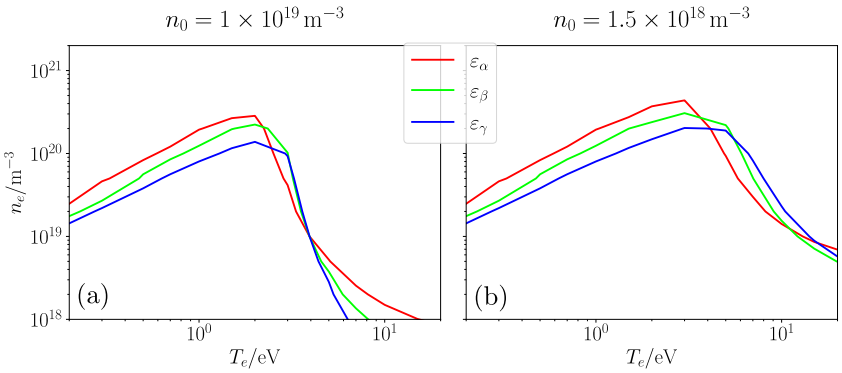

FIGURE 4.4: Situation from Fig. 4.3 (b) but assuming a δ distribution (a) instead of the range ±30 %. The determination of all three plasma parameters requires very small error bars since for a lower neutral density (b) the contours almost intersect.

4.3 Bayesian Inference of Plasma Parameters from Emissions

Inferring plasma parameters like in Fig. 4.3 (b) has the advantage of being simple and comprehensible. However, not all combinations of the inferred parameter values are equally likely. For example it is rather improbable that all three measurements are at the upper margin of the range. Thus, instead of intersecting areas we will multiply probabilities as it was conducted in [24]. At first we need to define probabilities given a single line $p(n_e, T_e|\varepsilon_{meas})$. For constant prior distributions[1] Bayes theorem reads

$$p(n_e, T_e|\varepsilon_{meas}) \propto p(\varepsilon_{meas}|n_e, T_e). \tag{4.3}$$

The probability of a certain combination of n_e and T_e is reflected by the probability that the emissions are $\varepsilon(n_e, T_e)$. It is assumed that ε_{meas} follows a normal distribution centered around $\varepsilon(n_e, T_e)$

$$p(\varepsilon_{meas}|n_e, T_e) = \frac{1}{\sqrt{2\pi\sigma^2}} \exp\left(-\frac{(\varepsilon_{meas} - \varepsilon(n_e, T_e))^2}{2\sigma^2}\right), \tag{4.4}$$

with a relative error $\sigma = \sigma_{rel}\varepsilon(n_e, T_e)$. This distribution is displayed in Fig. 4.5 given $\varepsilon_{meas} = 0.66\,\mathrm{kWm}^{-3}$ and $\sigma_{rel} = 15\,\%$ (a). Multiplying the distributions

[1] For the sake of a simple explanation. Actually $p(log(n_e), log(T_e))$ will be assumed constant for a reasonable parameter space.

for the D_α, D_β and D_γ lines yields (b). This is possible if the measurements are not correlated and is equivalent to the intersection done in Fig. 4.3.

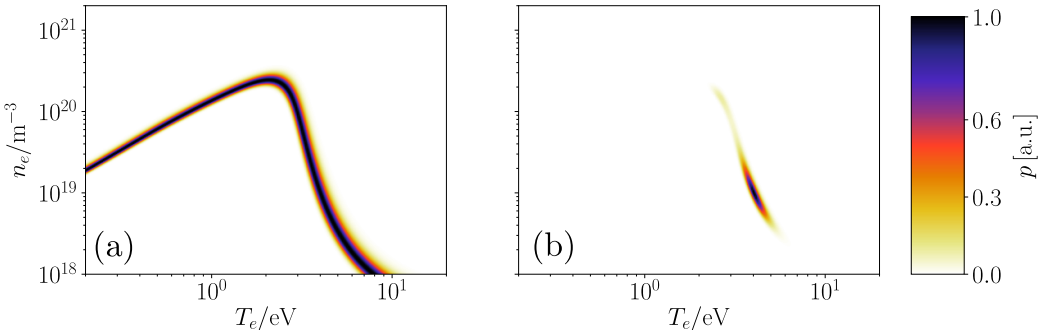

FIGURE 4.5: Replication of Fig. 4.3 but instead of the range ±30 % a Gauss distribution with $\sigma_{rel} = 15\,\%$ is assumed. The resulting 2D probability distribution $p(n_e, T_e)$ for $n_0 = 1 \times 10^{19}\,\mathrm{m}^{-3}$ and $\varepsilon_\beta = 0.66\,\mathrm{kWm}^{-3}$ is shown in (a), multiplying all the distributions for all three transitions results in (b).

If the third quantity is unknown, the probability distribution becomes three dimensional and hence difficult to visualize. However, it is possible to integrate the third dependency out. This is referred to as marginalization and can be obtained by adding distributions for various (log-sampled) neutral densities. The distribution for $n_0 = 2.0 \times 10^{18}\,\mathrm{m}^{-3}$ in Fig. 4.6 (a) and the distribution for $n_0 = 1.0 \times 10^{19}\,\mathrm{m}^{-3}$ in Fig. 4.5 (b) are part of the marginalized distribution in Fig. 4.6 (b).

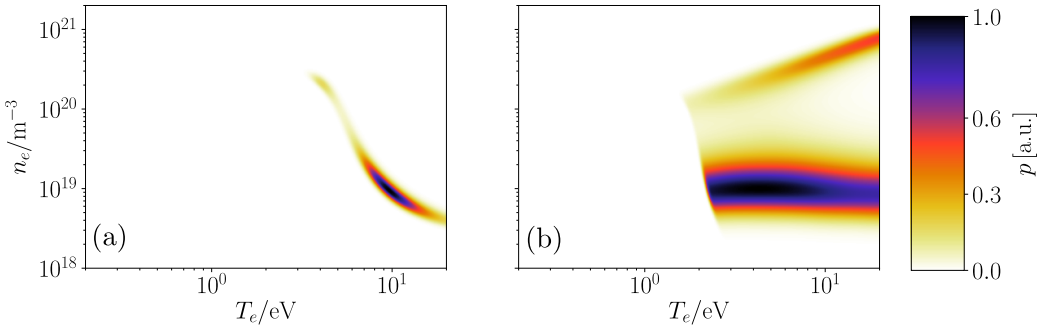

FIGURE 4.6: 2D probability distribution $p(n_e, T_e)$ given D_α, D_β and D_γ. Assuming a neutral density $n_0 = 2 \times 10^{18}\,\mathrm{m}^{-3}$ (a) and marginalized (b).

4.4 Testing with Simulated Data

In order to test the inference of plasma parameters in typical ASDEX Upgrade conditions, the SOLPS simulation of a partially detached L-mode has been

considered. However, any other distribution of plasma parameters could have been used for this test. Fig. 4.7 shows simulated plasma parameters, further details for a simulation of this discharge are given in [25]. Fig. 4.8 shows D_β emissions according to Eq. 4.1. While the D_β emissions are dominated by excitation, the relative amount of recombination increases for higher order transitions. For this simulation the relative amount of recombination on the integrated emissions is

$$\frac{P_{rec,\alpha}}{P_\alpha} = 0.8\,\% < \frac{P_{rec,\beta}}{P_\beta} = 3\,\% < \frac{P_{rec,\gamma}}{P_\gamma} = 10\,\%. \tag{4.5}$$

The magnitude of the emissions decreases with higher order transitions, for this simulation the overall emissions are

$$P_\alpha = 1.0\,\mathrm{kW} > P_\beta = 0.14\,\mathrm{kW} > P_\gamma = 21\,\mathrm{W}. \tag{4.6}$$

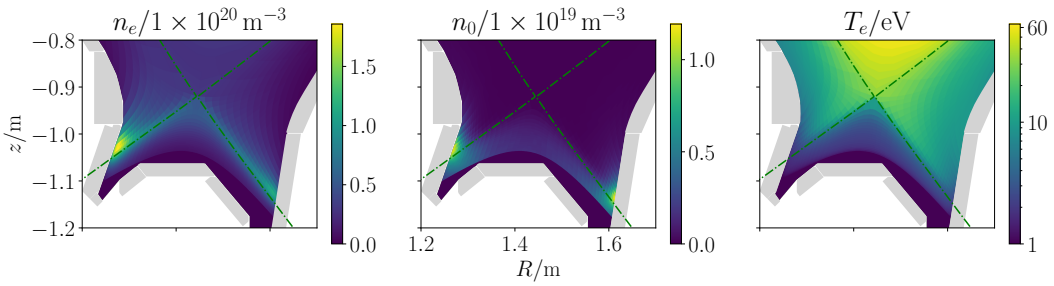

FIGURE 4.7: Simulated plasma parameters for AUG discharge #27100@2.8 s [25]. Electron and atomic neutral density, as well as electron temperature.

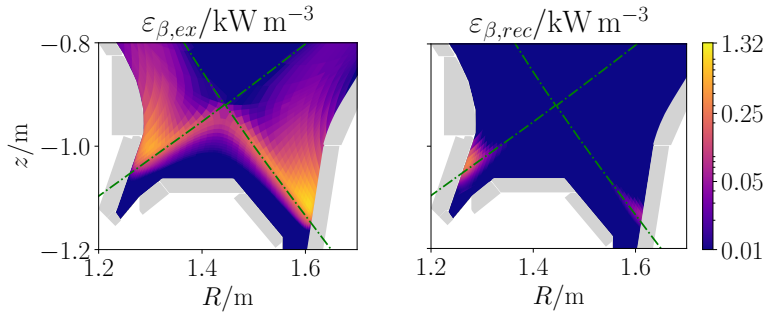

FIGURE 4.8: D_β excitation and recombination emissions for the simulation in Fig. 4.7.

In Sec. 3.2.4 the emissions of this simulation were forward modeled and then inverted. The reconstructed emissions and the correct 2D neutral density are used to determine 2D electron density and temperature. Therefore, the best matching plasma parameters are found by a brute force approach. The

quality of the match between plasma parameters and reconstructed emissions at some R, z is defined by

$$f(n_e, T_e) = \sum_{i=\alpha,\beta,\gamma} \frac{(\varepsilon_i(n_e, T_e) - \varepsilon_i(R, z))^2}{||\varepsilon_i||_\infty^2}, \tag{4.7}$$

where $||\varepsilon_i||_\infty$ is the maximum of $\varepsilon_i(R, z)$. The brute force approach means that for every voxel $f(n_e, T_e)$ is evaluated for many plasma parameters that might appear in the plasma edge. The values that yielded the smallest value are displayed in Fig. 4.9 next to the actual value of the simulation. Only those grid points are shown, where the relative error bar of the emissions did not exceed $\sigma_{rel} = 60\,\%$ for any of the three emission reconstructions. For simulated camera images the determination of 2D electron density and temperature works reasonably well for a given neutral density.

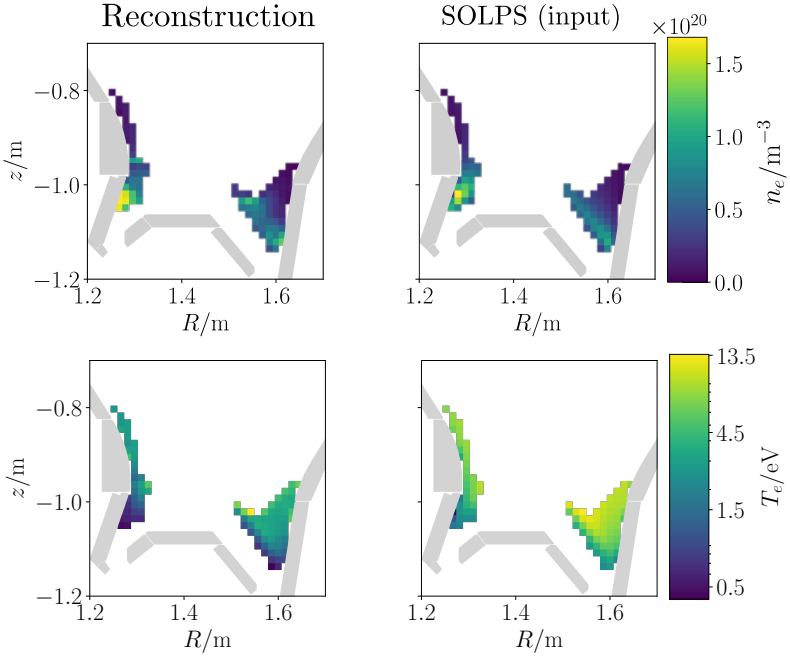

FIGURE 4.9: Reconstructing 2D plasma parameters from simulated camera images, using the 2D neutral density.

4.5 Testing with Experimental Data: ECRH Generated Plasmas

Filtered camera measurements of a technical plasma generated only by ECRH are introduced in Ch. 3.2.5 to reconstruct the distribution of emitted light. The reconstructions are used in this section to test the inference of plasma parameters experimentally. At the point of highest emissivity it is $\varepsilon_\alpha = 0.63\,\mathrm{kWm^{-3}}$,

$\varepsilon_\beta = 0.13\,\mathrm{kWm^{-3}}$ and $\varepsilon_\gamma = 0.044\,\mathrm{kWm^{-3}}$. Assuming an accuracy of ±30% for these emissions and a neutral density of $n_0 = 1.0 \times 10^{18}\,\mathrm{m^{-3}}$ limits possible values of the electron density and temperature to the black area in Fig. 4.10. For each individual Balmer transition recombination is dominant up to the point where the inferred density decreases with electron temperature. In Fig. 4.10 this point is evident as a kink. Therefore, the black area at high density represents a solution with significant excitation in D_α while D_γ is dominated by recombination. The electron density and temperature can be determined to be within this small area if the solution at low density can be excluded. This is motivated with interferometer measurements that show line integrated electron densities in the order of $10^{19}\,\mathrm{m^{-2}}$ with a LoS horizontally through the plasma. Assuming that the electron densities at the bright region are higher than the average density and regarding the length of the LoS of about 1 m yields that electron densities in the order of $n_e = 10^{18}\,\mathrm{m^{-3}}$ can be excluded.

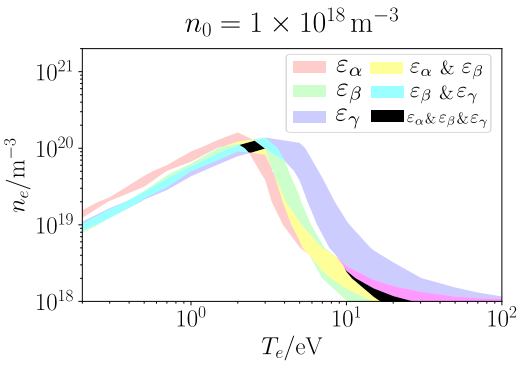

FIGURE 4.10: Inferred electron temperature and density of a plasma generated only by ECRH for $n_0 = 1.0 \times 10^{18}\,\mathrm{m^{-3}}$.

The choice for the neutral density $n_0 = 1.0 \times 10^{18}\,\mathrm{m^{-3}}$ is a rough estimate, but the marginalized distribution in Fig. 4.11 (a) shows that the high density solution only weakly depends on the neutral density. The high density solution corresponds to the branch at lower electron temperature in Fig. 4.11 (b) that also weakly depends on the neutral density. For a neutral density of about $n_0 = 2 \times 10^{17}\,\mathrm{m^{-3}}$ the low electron density solutions reach up to $n_e = 10^{19}\,\mathrm{m^{-3}}$. Following Fig. 4.11 (b) such low neutral densities correspond to very high electron temperatures of $T_e > 100$ eV. Furthermore, a neutral density of $n_0 = 2 \times 10^{17}\,\mathrm{m^{-3}}$ at the resonance is small compared to baraton measurements outside the main chamber at the midplane. These show a neutral gas pressure of 3×10^{-2} Pa for #39142@0.46s which yields molecular densities of $7 \times 10^{18}\,\mathrm{m^{-3}}$ when using the ideal gas law n=p/(kT) at room temperature. Pressure gauge measurements confirm molecular densities of $10^{18} - 10^{19}\,\mathrm{m^{-3}}$ which further reduces the likelihood of $n_e \approx 10^{19}\,\mathrm{m^{-3}}$ and the low density solution can be neglected. Since the high density solution shows a weak dependence on the neutral density it is approximately $n_e \approx 1 \times 10^{20}\,\mathrm{m^{-3}}$ and $T_e = 2.5 \pm 1.5$ eV at the point of highest emissivity.

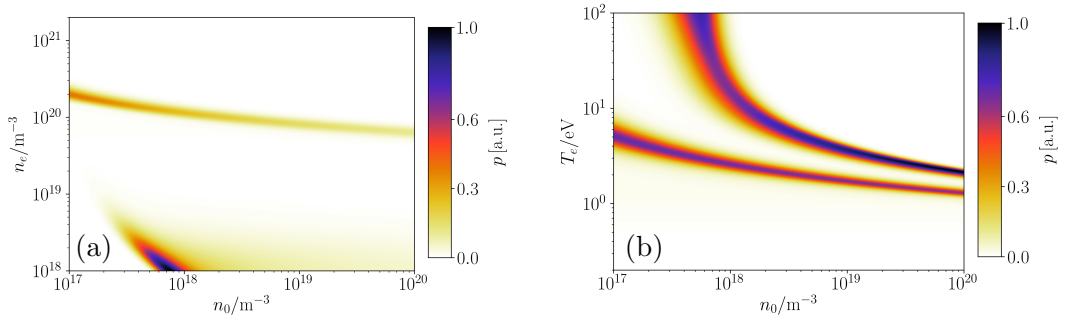

FIGURE 4.11: Bayesian inference for the same emissions used for Fig. 4.11 with marginalized electron temperature (a) and density (b). The inferred electron temperature and density in decrease slowly with neutral density.

To determine 2D parameters in an automatized way a brute force method will sometimes find the low density solution. It is possible to limit the range of possible plasma parameters or assign prior probabilities. Another solution is to use gradient based optimization algorithms starting at $n_e = 1 \times 10^{20}\,\mathrm{m}^{-3}$ and $T_e = 3\,\mathrm{eV}$. The Nelder-Mead algorithm [22] proved to find the local minimum of Eq. 4.7 reliably. The resulting 2D electron density and temperature are shown in Fig. 4.12. The electron temperature is shown at the emission peak, these are voxel where the relative uncertainty did not exceed $\sigma_{rel} = \varepsilon/\Sigma_{\varepsilon|\Phi} = 60\,\%$ for each of the transitions. While the electron density is not necessarily close to zero away from the emission peak, the shown 2D electron density profile compares in order of magnitude to interferometer measurements since integrating the 2D electron density profile on the interferometer LoS yields $0.6 \times 10^{19}\,\mathrm{m}^{-2}$. However, this method should only be applied if the range of possible plasma parameters is small. For some ECRH generated plasmas this was not the case.

Comparing the GPT reconstruction to an approach using minimum Fisher regularization (with code described in [26]) yields that accuracies of 30 % are achievable. Simulations with the 1D transport code Tomator show small molecular densities at the resonance, supporting the assumption to neglect plasma-molecule interaction [27]. It remains to be shown if the density profile is indeed so peaked. Interferometer measurements along a vertical LoS with length 2.3 m that is not passing the resonance show line integrated densities in the order of $2 \times 10^{18}\,\mathrm{m}^{-2}$ for similar experiments in another tokamak. [28] Thomson scattering measurements in a third tokamak indicated higher temperatures of about $T_e = 20 - 40\,\mathrm{eV}$ and electron densities of $1.5 \times 10^{19}\,\mathrm{m}^{-3}$. [29] However, simulations with the 1D transport code Tomator indicate $T_e = 2.5\,\mathrm{eV}$ at peak densities of $n_e = 2 - 12 \times 10^{19}\,\mathrm{m}^{-3}$ [27]. Possibly these low temperatures come with a non-Maxwellian tail that is relevant for the ionization of the plasma, but at this point the test for the inference of plasma parameters cannot be falsified. It remains up to future work to decide if the observed emissions appear due to density peaking or the uncertainties are larger and the emissions originate from excitation that appears due to temperature peaking.

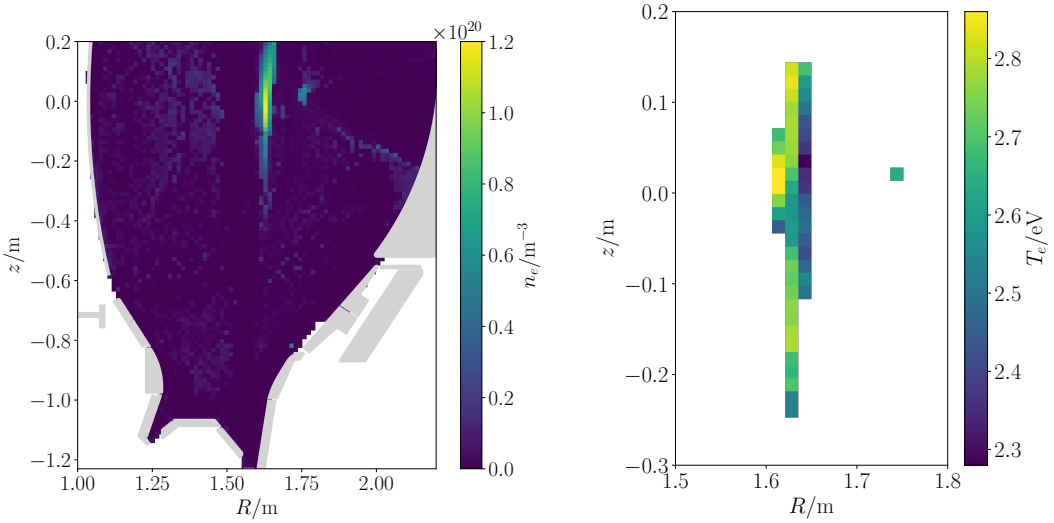

FIGURE 4.12: Testing the inference of plasma parameters for AUG "discharge" #39142@0.47s, a plasma generated only by electron cyclotron resonance heating. Determined 2D electron density and temperature represent a local minimum of Eq. 4.7.

Chapter 5

An Application to the X-Point Radiator Regime in ASDEX Upgrade

The X-point radiator (XPR) regime is characterized by a radiated power density in the order of 10^7 Wm^{-3} in the confined region near the X-point. This can be seen in a tomographic reconstruction of the radiated power in Fig. 5.1 that is based on bolometer measurements. The regime is considered reactor relevant since up to 90 % of the power exhaust can be radiated at a high confinement. Once reaching a certain height, a well-developed XPR can counteract the steepening of the pressure gradient such that ELMs are suppressed while remaining in H-mode.

An XPR can be obtained with low-Z impurities like nitrogen or argon that radiate a significant amount of power well below temperatures of 20 eV. Further away from the X-point, but on the same flux surface, temperatures are thought to be in the order of 100 eV. It is rather surprising that such steep parallel temperature gradients represent a stable configuration.

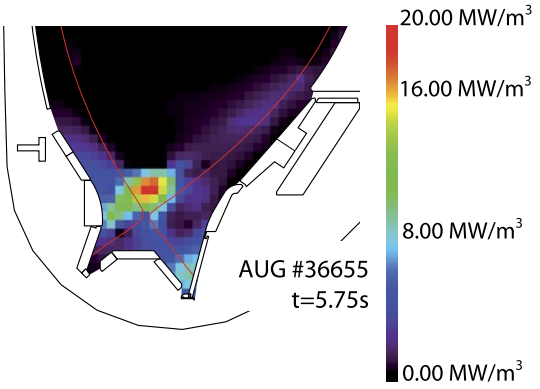

FIGURE 5.1: Tomographic reconstruction of radiated power showing the X-point radiator in AUG discharge #36655@5.75 s. Figure adapted from [30].

Filtered camera images of two discharges are evaluated in Sec. 5.1. For

the analysis in this thesis the dedicated discharge #38486 ($B_t = 2.5$ T) was performed in H-mode featuring real time control of the XPR height. It can be seen in Fig. 5.2 that feedback seeding of nitrogen [30] was used to control the vertical position of the XPR with bolometer measurements and set it 10 cm above the X-point. When reaching a height of about 9 to 10 cm at 5.0 s ELMs disappeared. Due to its stability the XPR in #38486@5.1 s is well suited for the analysis with filtered cameras. The second discharge #38773@5.6 s has similar external parameters such as a plasma current of 0.8 MA, deuterium seeding of $2.2 \times 10^{22}/\,\mathrm{s}$ and 10 MW supplied heating power. Apart from a different strike point position #38486 comes with a smaller toroidal magnetic field, it is 1.8 T instead of 2.5 T. The results are compared to other diagnostics and a SOLPS simulations in Sec. 5.2.

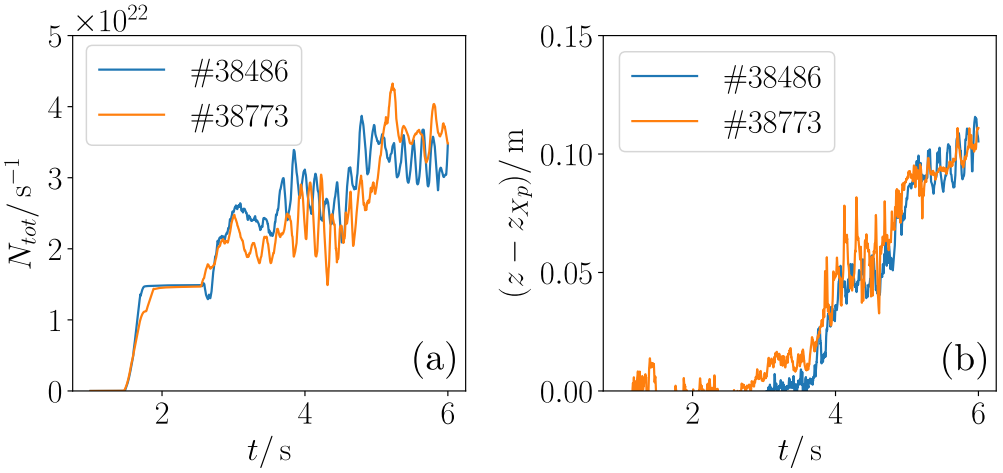

FIGURE 5.2: Nitrogen seeding in electron equivalent (a) is used to control the vertical position of the XPR above the X-point (b). Signals are slightly smoothed.

5.1 Camera Diagnostics

A reconstruction of the D_β emissions of AUG discharge #38486@5.1 s is shown in Fig. 5.3 (a). The white dashes in Fig. 5.3 (a) indicate the divertor Thomson scattering volumes. To compare the diagnostics, the rightmost DTS scattering volume in the confined region is regarded. The reconstructed emissions at this position are $\varepsilon_\alpha = 12\,\mathrm{kWm}^{-3}$, $\varepsilon_\beta = 3.8\,\mathrm{kWm}^{-3}$ and $\varepsilon_\gamma = 1.6\,\mathrm{kWm}^{-3}$. To infer plasma parameters it is estimated that the actual emissions are within a factor two of these values $1.9\,\mathrm{kWm}^{-3} < \varepsilon_\beta < 7.6\,\mathrm{kWm}^{-3}$, which is motivated with a very first comparison to divertor spectroscopy. The ranges for all three transitions limit possible n_e and T_e for various fractions of the neutral density n_0/n_e to the black area in Fig. 5.4. Neglecting plasma-molecule interaction is a good assumption for the XPR since the mean free path through the plasma is small.

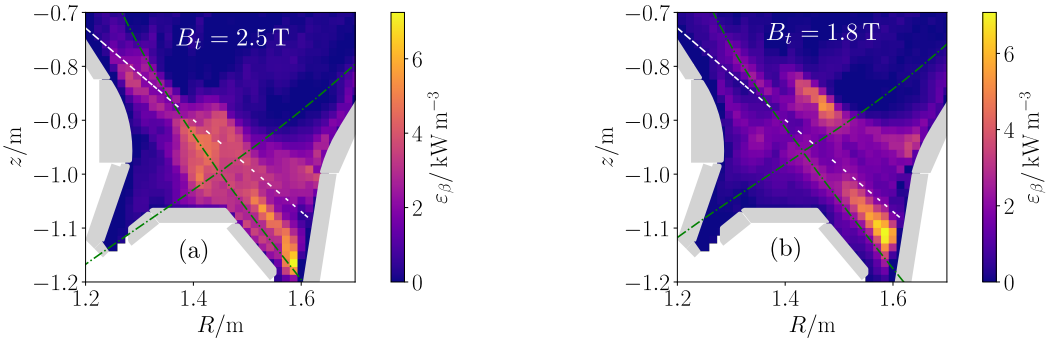

FIGURE 5.3: Inversions of the camera measuring D_β for AUG discharge #38486@5.1 s (a) and AUG discharge #38773@5.6 s (b).

It is supported by EMC3-Eirene simulations of XPR discharges that this leads to a significant molecular density of hydrogen only close to the wall. For each individual Balmer transition recombination is dominant up to the point where the inferred density decreases with electron temperature. In Fig. 4.10 this point is evident as a kink and occurs at lower temperatures for D_α than for D_γ. The three measurements do not intersect for temperatures above the D_γ kink which reflects that the emissions are dominated by recombination. There is a small range of possible parameters beyond the D_α kink at the highest temperatures of the black area. There ε_α is at the upper and ε_γ is at the lower margin, resulting in a line ratio that is up to four times the measurement. Since the emission ratios can be determined with a higher accuracy than the absolute value it can be approximated that the three measurements do not intersect for temperatures above the kink. Therefore, the emissions of the three transitions are dominated by recombination at temperatures $T_e < 10$ eV and densities $n_e < 1 \times 10^{21}\,\mathrm{m^{-3}}$. The upper limits are smaller for higher neutral densities, but for either case the temperature further upstream is significantly higher. The obtained range can be compared to the conditions further upstream, where the temperature is significantly higher. Therefore, this is among the first experimental findings indicating strong parallel gradients in the confined region.

In Fig. 5.3 (b) reconstructed D_β emissions of AUG discharge #38773@5.6 s are displayed. While the camera measuring D_γ shows a similar emission pattern, no ε_α is evident within the confined region. Since it is difficult to explain such a finding with Balmer emissions the observed XPR emissions might be from nitrogen. A possible explanation that Balmer emissions are less significant is associated to a shorter connection length that appears with a smaller toroidal field. The connection length affects the heat conduction and thus the XPR temperature. The lacking recombination emissions would therefore be explained with the increasing radiated power of nitrogen. In contrast to Fig. 5.3 (a) the observed emissions appear further away from the X-point towards the outboard midplane. Bolometric measurements for various discharges show a tendency of the XPR to develop in this direction as well.

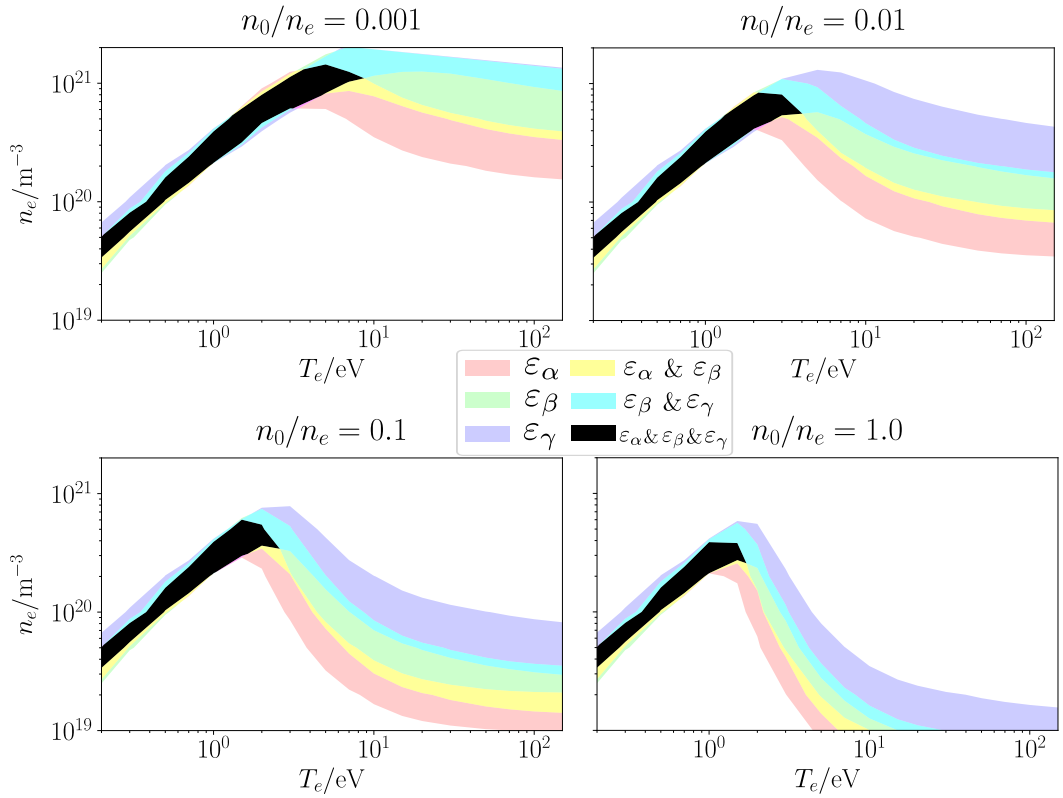

FIGURE 5.4: Inference of possible plasma parameters for various fractions of the neutral density using $6\,\mathrm{kWm}^{-3} < \varepsilon_\alpha < 24\,\mathrm{kWm}^{-3}$, $1.9\,\mathrm{kWm}^{-3} < \varepsilon_\beta < 7.6\,\mathrm{kWm}^{-3}$ and $3.2\,\mathrm{kWm}^{-3} < \varepsilon_\gamma < 0.8\,\mathrm{kWm}^{-3}$. Since the three measurements intersect where the density is increasing with temperature, the emissions are dominated by recombination.

5.2 Other Diagnostics and Simulation

For AUG discharge #38486@5.1 s measurements of the rightmost divertor Thomson scattering (DTS) volume in the confined region show electron temperatures of $T_e \approx 1.0$ eV at densities of $n_e \approx 1.7 \times 10^{20}\,\mathrm{m}^{-3}$. If the emissions are dominated by recombination the DTS measurement allows to calculate $\varepsilon_\beta = 1.1\,\mathrm{kWm}^{-3}$. Also for ε_α and ε_γ the reconstructed emissions from the cameras are about a factor of three higher supporting that the ratios can be determined more accurately. For any of the four neutral fractions in Fig. 5.4 the electron density at $T_e = 1$ eV ranges from $2.1 \times 10^{20}\,\mathrm{m}^{-3}$ to $3.9 \times 10^{20}\,\mathrm{m}^{-3}$, this is only slightly larger than the DTS measurement due to the non linear dependency.

The LoS of divertor spectroscopy shown in Fig. 2.3 (b) do not cover the emissions peak that is evident in the confined region of Fig. 5.3 (b). Therefore, divertor spectroscopy cannot be used to check if these are nitrogen emissions. However, it is possible to integrate the reconstructions from the camera data on the divertor spectroscopy LoS and verify the order of magnitude with divertor

spectroscopy measurements. For AUG discharge #38773@5.6 s the deviation was less than a factor of two.

A SOLPS simulation of the X-point radiator regime is challenging due to non-linear dependencies on the volumetric processes. Two SOLPS simulations of AUG discharge #38773@5.6 s were successfully conducted by Dr. Ou Pan. The emissions in Fig. 5.5 were calculated from the simulations using the generalized collisional-radiative model described in Ch. 4.1. It can be seen that the X-point radiator may (a) or may barely be visible (b) in hydrogen Balmer emissions. Therefore, it cannot finally be concluded if the observed emissions in Fig. 5.3 (b) are from nitrogen. The nitrogen seeding rate used for the simulation is $2 \times 10^{21}/\,\mathrm{s}$ electron equivalent for (a), but only $1 \times 10^{21}/\,\mathrm{s}$ for the simulation in (b). Resulting temperatures in the confined region of (b) reach down to $T_e = 3$ eV, but the higher nitrogen seeding in (a) results in temperatures as low as $T_e = 1.3$ eV. Integrating the Balmer emissions in Fig. 5.5 (a) over the whole plasma volume yields $P_\beta = 1.3\,\mathrm{kW}$, 90 % of these emissions are from recombination. Also for the other Balmer transitions the emissions are dominated by recombination

$$\frac{P_{rec,\alpha}}{P_\alpha} = 74\,\% < \frac{P_{rec,\beta}}{P_\beta} = 90\,\% < \frac{P_{rec,\gamma}}{P_\gamma} = 96\,\%. \tag{5.1}$$

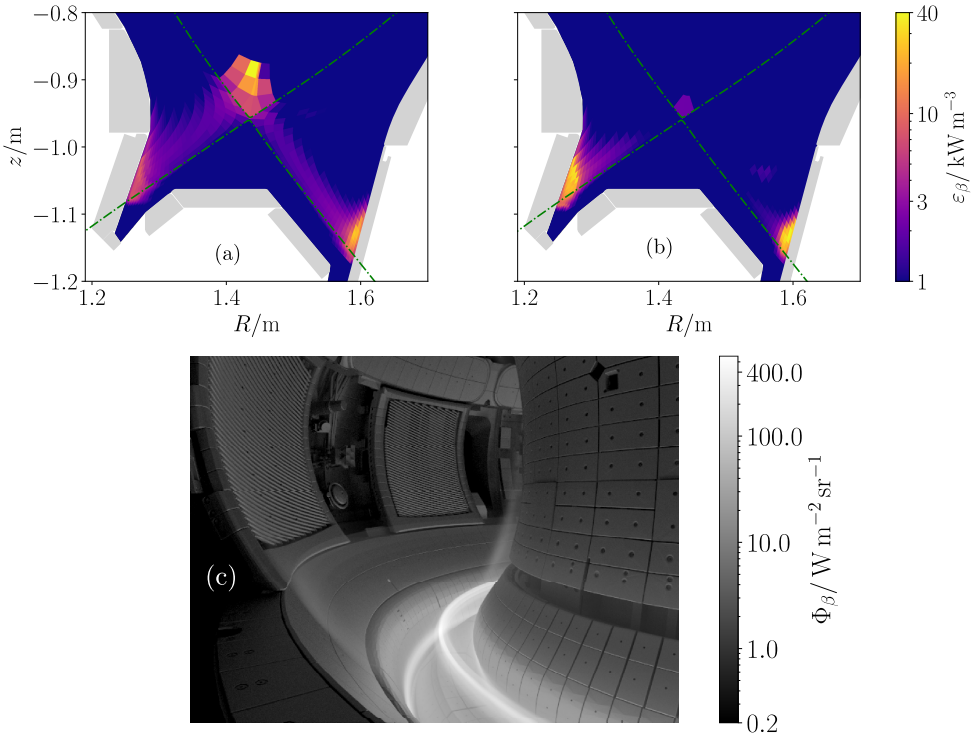

FIGURE 5.5: Hydrogen Balmer D_β emissions for two SOLPS simulations of AUG discharge #38773@5.6 s, courtesy of Dr. Ou Pan. The XPR is well visible in the forward modeled image (c) of the emissions in (a). For simulation (b) the nitrogen seeding was only halve the value of simulation (b). Hence the XPR is not as cold and the Balmer emissions are insignificant. Only simulation (b) could explain that the XPR is not visible in D_α.

Chapter 6

Summary and Outlook

A method for the determination of 2D plasma parameter profiles has been developed and tested in this thesis. The analysis method consists of three essential steps: calibration, tomographic reconstruction and inference of plasma parameters. It may serve as a diagnostics for tokamak plasmas at positions that are not easily accessible to in-situ measurement devices like Langmuir probes. The method makes use of filtered camera images observing visible light from the plasma. Due to the large number of line integrated measurements (in the order of 10^5), the spatial resolution is high. However, due to a complex viewing geometry and reflection of light on wall surfaces, these images are difficult to interpret. The problem of the reflections is particularly challenging in ASDEX Upgrade since the material of the plasma facing surfaces is tungsten. While such camera measurements are available since many years, recent developments in available computing power facilitate the analysis substantially.

The filtered cameras are calibrated in a first step, highlighting the need for a precise absolute and geometric calibration. Not only due to the limited space in a tokamak, but also due to the harsh environment with neutron radiation and electromagnetic activity it is non-trivial to carry out high quality camera measurements in such a device. As opposed to other systems, where ordered fiber bundles are used to guide the image to the camera, particularly robust cameras were operated in close vicinity of the plasma for this thesis. While their image quality is particularly high, a filter dependence on the angle of incidence is introduced.

In a second step, the toroidally symmetric distribution of the emitted light is reconstructed from the line integrated camera measurements. Therefore, an accurate model to describe the geometry of the camera is needed. In addition to a precise geometric calibration, 3D construction drawings are used to model photo-realistic reflections with the CHERAB-framework. In an innovative approach such a complex forward model could be inverted using Gaussian process tomography. The inversion is defined by only three scalars that describe uncertainties and can be optimized for the measurement in an automatized way.

The reconstruction has been tested on data from 2D simulations using the

scrape-off layer transport code SOLPS. While the method is found to be accurate, difficulties were encountered close to the wall. In general, it seems difficult to reconstruct emissions that are not standing out when inspected by human eye. Nevertheless, the tomographic reconstruction is useful to locate outstanding emissions and approximate their structure and magnitude. The total emitted power of the Balmer lines in the simulation could be reconstructed precisely. The tomographic reconstruction method was applied to a technical low temperature plasma generated by electron cyclotron resonance heating (ECRH) for wall conditioning purposes. The observed plasma was particularly well suited for reconstruction because the maximum emitted light was far away from the wall.

Finally, plasma parameters are inferred from these tomographic reconstructions. This is possible using known photon emissivity coefficients for the hydrogen Balmer α, β and γ spectral lines as a function of plasma parameters. For the simulation of a partially detached L-mode plasma 2D electron temperature and density profiles were reconstructed. Due to the similarity of the photon emissivity coefficient this required fixing the 2D neutral density profile. The feasibility to determine 2D electron density and temperature profiles experimentally is tested for a technical low temperature plasma generated only by electron cyclotron resonance heating.

The method was furthermore applied to dedicated discharges with a well developed X-point radiator (XPR). Emissions from the X-point region could be observed and are well suited for the analysis because the X-point is far away from the wall. The presented analysis of a first discharge indicates that a well developed XPR cools the plasma to a point where recombination dominates the measured Balmer line emissions at temperatures $T_e < 10$ eV. A second discharge with a lower toroidal field showed a different emission pattern. The region close to the X-point appears dark where strong Balmer emissions were observed in the first discharge, but there are emissions away from the X-point towards the outboard midplane.
It is highlighted that these are among the first experimental findings indicating strong electron temperature and density gradients on closed flux surfaces. Further studies are needed to understand how the immense temperature drop is related to the onset of ELM suppression. Also, low temperatures may have consequences for the local toroidal plasma current distribution in the X-point region. Made observations confirm the tendency of the XPR to develop in direction of the outboard midplane, further studies might deliver insights to XPR instability towards the inward midplane. In summary, a powerful method was developed and tested to diagnose the details of the X-point radiator regime.

Appendix A

Optical Inference Filters

A.1 Perpendicular Incidence

Optical inference filters implement thin films to form optical cavities, also known as resonators. To keep the analysis of this system simple the magnetic permeability shall be 1 everywhere and refractive indices are real valued, i.e. no absorption. Furthermore the used materials shall not exhibit dispersion, i.e. refractive indices do not depend on wavelength. The principle of multi-layer optical inference shall be explained by means of the Bragg mirror. It is used to reflect a particular wavelength λ_d very well, while a bandpass filter transmits a particular wavelength. But the principle is similar[1].

A Bragg mirror consists of thin films with alternating refractive index, this is illustrated in Fig. A.1. The film layers have a thickness $d_i = \lambda_d/(4n_i)$, where n_i is its refractive index and λ_d its design wavelength, here 1000 nm. It is shown that the design wavelength does not penetrate the mirror, but is reflected at the air interface on the right. The wave with $\lambda = 800\,\text{nm}$ is only partially reflected and develops a complicated interference pattern.

The degree of transmission at each layer interface is given by the Fresnel equations. Let us consider the partial transmission at an interface from medium 1 to medium 2. This process is time symmetric, so reversing the arrow of time must lead to the initial situation. When reflecting in the medium of low refractive index a $\lambda/2$ phase shift is introduced. This enables destructive interference in medium 2, when rewinding the process. To annihilate both intensities must match up. Therefore the transmission is $T_{1\to2} = T_{2\to1}$[2].

The Bragg mirror consists of two media with n_{high} and n_{low}. The transmission is constant for every layer interface. There is a $\lambda/2$ phase shift when reflecting in n_{low}. The reflectivity is low, but there are many interfaces.

To get a high overall reflection every back-propagating wave must interfere constructively. Let us consider the first two layers and disregard the air

[1] A Fabry-Pérot interferometer does transmit the design wavelength. However, its use of single-layer interference makes it misleading to compare it to the used filters.

[2] Indeed, the Fresnel equations obey $T_i(\theta_1, \theta_2, n_1, n_2) = T_i(\theta_2, \theta_1, n_2, n_1)$, where i represents any polarization.

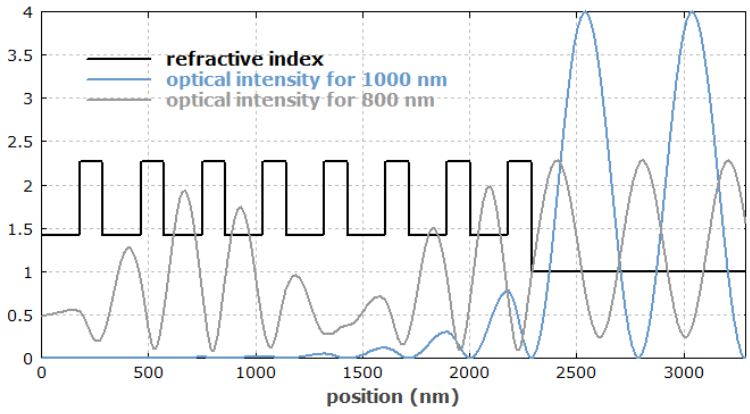

FIGURE A.1: Interference pattern at the surface of a Bragg mirror according to [31].

interface. The reflection at the first interface introduces no phase shift. The reflection at the second interface is at low refractive index and consequently introduces a phase shift of $\lambda/2$. The reflection at the second interface has an additional optical path of

$$\Delta_\perp = 2d_{low}n_{low} = \lambda_d/2 \tag{A.1}$$

because of propagation and back-propagation. Thus, the two reflections interfere constructively for $\lambda = \lambda_d$.

Considering a reflection in the third layer the missing $\lambda/2$ phase shift makes up for the additional $\lambda_d/2$ optical path difference. Thus all back-propagating waves interfere constructively. The behavior for other wavelengths than λ_d, such as $\lambda = 800\,\text{nm}$, will depend on the refractive contrast n_{high}/n_{low} and on the number of layers. [31]

A.2 Derivation Wavelength Shift

Using optical resonance inherently leads to a dependence on the angle of incidence θ. The afore described interference of two back-propagating waves will now be discussed under a small angle of incidence. This will introduce a phase shift for the reflection at the first interface.

Fig. A.2 shows the relevant paths. The reflection at the second interface introduces a height difference h. This makes it necessary to introduce a new optical path for the reflection at the first interface (magenta, solid). Its relative phase shift can be constructed by means of an optical path difference Δ_1 (green, dash-dotted). Trigonometric and optical considerations yield $\Delta_1 = n_{high}sin\theta' h$ and $tan\theta'' = \frac{h}{2}/\frac{\lambda_d}{4n_{low}}$. Combining both with Eq. A.1 and Snell's law[3] yields

$$\Delta_1 = tan\theta'' sin\theta'' \Delta_\perp. \tag{A.2}$$

[3] $\sin\theta''/\sin\theta' = n_{low}/n_{high}$

In contrast, the length of the optical path due to reflection at the second interface (blue, dashed) also increases to

$$\Delta_2 = \Delta_\perp / cos\theta'' + \lambda_d/2. \tag{A.3}$$

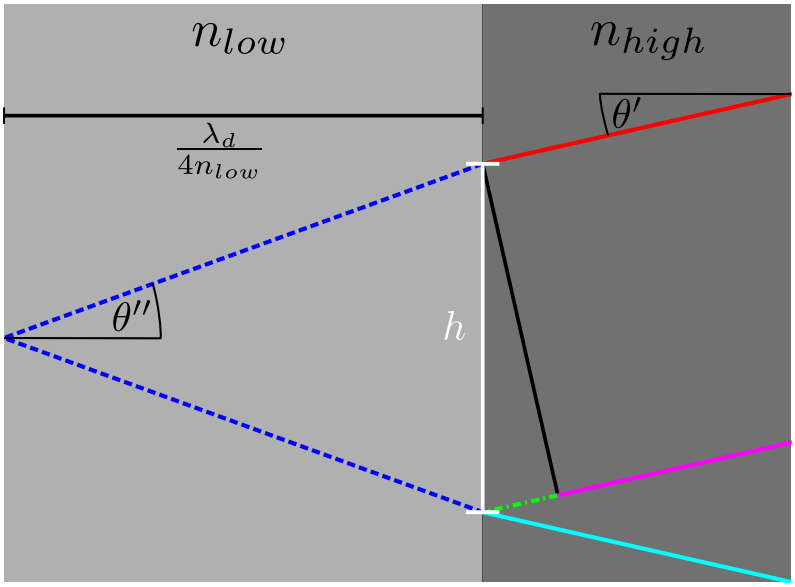

FIGURE A.2: Ideal optical resonance in two layers. Two optical paths for light incoming from the right (red, solid) and (magenta solid). For constructive interference (blue, solid) both paths have a path . Δ_2 due to reflection at the second interface (blue, dashed). Incoming path of the latter (red, solid). Δ_1 due to a vertical shift h (green, dash-dotted). Incoming path of the latter that is not relevant for a phase shift (magenta, solid).

The overall optical path difference is $\Delta = \Delta_2 - (\Delta_1 + \lambda/2)$. Inserting Eq. A.2 and Eq. A.3 for $\lambda_d = \lambda$ yields

$$\frac{\Delta}{\Delta_\perp} = \frac{1}{cos\theta''} - tan\theta'' sin\theta'' = cos\theta''. \tag{A.4}$$

There is also the reversed situation if the incoming path is at low refractive index and the optical path difference decreases by $cos\theta'$. Thus ideal resonance under an angle is not possible. The best reflectivity will be at

$$\frac{\Delta}{\Delta_\perp} = \frac{cos\theta'' + cos\theta'}{2} = \frac{\sqrt{1 - \frac{sin^2\theta}{n_{low}^2}} + \sqrt{1 - \frac{sin^2\theta}{n_{high}^2}}}{2}, \tag{A.5}$$

where Snell's law was used for the second step. The wavelength shift will behave accordingly.

This can be approximated by

$$\frac{\Delta}{\Delta_\perp} = \sqrt{1 - \frac{\sin^2\theta}{n^2}} + \mathcal{O}(\theta^4) \tag{A.6}$$

to get Eq. 2.1. Comparing coefficients of the series expansions yields

$$n = \sqrt{\frac{2}{n_{low}^{-2} + n_{high}^{-2}}}. \tag{A.7}$$

Bibliography

[1] *World Energy Outlook 2021* (International Energy Agency, Paris, 2021).

[2] What is the source of the electricity we consume?: https://ec.europa.eu/eurostat/cache/infographs/energy/bloc-3b.html, 2021.

[3] The Tao of Q: https://www.iter.org/newsline/-/2845, 2021.

[4] J. W. Connor, A. Kirk, and H. R. Wilson, AIP Conf. Proc. **1013**, 174 (2008).

[5] ASDEX Team, Nucl. Fusion **29**, 1959 (1989).

[6] J. Harhausen, Ph.D. thesis, Ludwig-Maximilians-Universität München, 2009.

[7] M. Agostini *et al.*, Plasma Phys. Controlled Fusion **61**, 115001 (2019).

[8] A. Perek *et al.*, Nuclear Materials and Energy **26**, 100858 (2021).

[9] T. Ravensbergen *et al.*, Nat. Commun. **12**, 1 (2021).

[10] C. Bowman *et al.*, Plasma Phys. Controlled Fusion **62**, 045014 (2020).

[11] ASDEX Upgrade: Detailed description of ASDEX Upgrade: https://www.aug.ipp.mpg.de/wwwaug/documentation/physics/techdata.shtml, 2021.

[12] B. Kurzan *et al.*, Design and first measurements of the divertor Thomson scattering system on ASDEX Upgrade, 2021.

[13] B. Kurzan *et al.*, J. Instrum. **16**, C09012 (2021).

[14] S. Potzel *et al.*, Plasma Phys. Controlled Fusion **56**, 025010 (2014).

[15] S. Silburn *et al.*, Calcam: https://doi.org/10.5281/zenodo.4698377, 2021.

[16] M. Carr *et al.*, Rev. Sci. Instrum. **90**, 043504 (2019).

[17] M. Carr *et al.*, in *Towards integrated data analysis of divertor diagnostics with ray-tracing* (pure.mpg.de, Waterside Centre in Belfast, 2017).

[18] K. Munechika, H. Tsutsui, and S. Tsuji-Iio, Plasma and Fusion Research **16**, 2402033 (2021).

[19] D. Li *et al.*, Rev. Sci. Instrum. **84**, 083506 (2013).

[20] K. Moser, Bachelor's thesis, LMU Munich, 2020.

[21] W. von der Linden, V. Dose, and U. von Toussaint, *Bayesian Probability Theory: Applications in the Physical Sciences* (Cambridge University Press, Cambridge, England, UK, 2014), pp. 431–450.

[22] P. Virtanen *et al.*, Nature Methods **17**, 261 (2020).

[23] H. P. Summers *et al.*, AIP Conf. Proc. **901**, 239 (2007).

[24] T. Nishizawa *et al.*, Plasma Phys. Controlled Fusion **62**, 085005 (2020).

[25] H. Wu *et al.*, Plasma Phys. Controlled Fusion **63**, 105005 (2021).

[26] J. Svoboda *et al.*, J. Instrum. **16**, C12015 (2021).

[27] T. Wauters *et al.*, in preparation for Nucl. Fusion (2022) .

[28] G. L. Jackson, J. S. DeGrassie, C. P. Moeller, and R. Prater, Nucl. Fusion **47**, 257 (2007).

[29] D. Douai *et al.*, Nucl. Fusion **58**, 026018 (2017).

[30] M. Bernert *et al.*, Nucl. Fusion **61**, 024001 (2021).

[31] Dr. R. Paschotta, Bragg Mirrors: https://www.rp-photonics.com/bragg_mirrors.html, 2021.

Acknowledgments

First and foremost I would like to thank my supervisors Dr. Marco Cavedon, who is additionally credited for the idea of this thesis, and Dr. Tilmann Lunt for the exceptional amount of effort put into my proceeding. I would also like to thank Professor Dr. Ulrich Stroth for giving me the opportunity to develop this approach.

In general I highly appreciated the positive atmosphere at the institute and would like to express my thanks for all the support that I have received. The discussions with Dr. Matthias Bernert on the X-point radiator were most interesting. Moritz Gruber is a technician with foresight and passion who was always ready to help. I would like to thank Dr. Ou Pan for providing SOLPS simulations, Dr. Takashi Nishizawa for his code and expertise on Bayesian inference, Dr. Udo von Touissant for his expertise on inverse problems and Dr. Pierre David for his considerations on cameras. To my fellow students, it was a pleasure to meet you.